Paramagnetic Pyrazolylborate Complexes, Tp_2M and Tp^*_2M. ^1H, ^{13}C, ^{11}B, and ^{14}N NMR Spectra and First-Principles Studies of Chemical Shifts

Ari Pyykkönen, Robert Feher, Frank H. Köhler,* and Juha Vaara*

Abstract

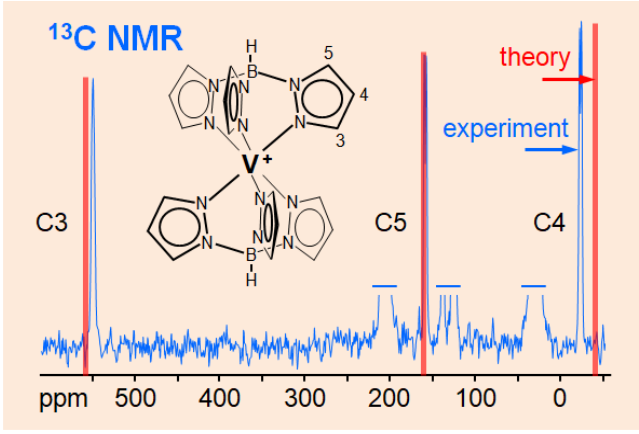

Paramagnetic pyrazolylborates Tp_2M and Tp^*_2M (M = Cu, Ni, Co, Fe, Mn, Cr, V) as well as $[Tp_2M]^+$ and $[Tp^*_2M]^+$ (M = Fe, Cr, V) have been synthesized and their NMR spectra recorded. The ^1H signal shift ranges vary from ~30 ppm [Cu(II) and V(III)] to ~220 ppm [Co(II)] and the ^{13}C signal shift ranges from ~180 ppm [Fe(III)] to ~1150 ppm [Cr(II)]. The ^{11}B and ^{14}N shifts are ~360 ppm and ~730 ppm, respectively. Both negative and positive shifts have been observed for all nuclei. The narrow NMR signals of the Co(II), Fe(II), Fe(III), and V(III) derivatives provide resolved ^{13}C,^1H couplings. All chemical shifts have been calculated from first-principles calculations on a modern version of Kurland-McGarvey theory which includes optimized structures, zero-field splitting- and *g*-tensors, as well as signal shift contributions. Temperature dependence in the Fe(II) spin-crossover complex results from the equilibrium of the ground singlet and the excited quintet. We illustrate both the assignment and analysis capabilities, as well as the shortcomings of the current computational methodology.

INTRODUCTION

The chemistry of poly(pyrazolyl)borate ligands is a success story with hydrotris(pyrazolyl)borate (Tp) at the outset.[1] These ligands owe their popularity to often convenient syntheses, to the formation of stable, generally chelating metal-ligand bonds such as neutral and ionic Tp_2M (Figure 1a), and to the fact that the bonding may be tuned in a wide range by appropriately substituting the pyrazolyl fragments (2. generation Tp) and the boron cap (3. generation Tp).[2,3,4] They bind to virtually all metal ions, preferably to transition metal ions which are often paramagnetic and thus yield a plethora of open-shell derivatives. Such pyrazolylborate complexes and their congeners figure as model compounds in bioinorganic chemistry,[5,6] they have been used to fix small molecules,[7,8] they may exhibit spin crossover,[9] and they are building blocks for assembling molecular

magnets.[10,11,12] Other promising application fields of pyrazolylborate complexes are catalysis[13,14,15,16,17] and the incorporation into polymers,[18] dendrimers,[19] molecular machines,[20] and metal-organic frameworks.[21]

From the very first, these compounds have been studied by using paramagnetic NMR spectroscopy (pNMR)[1,22,23,24] and the initial results have been compiled.[25] Note that in the early literature the signs of pNMR signal shifts are inverted. Subsequent work, which shall be referred to below, is based on those findings and usually limited to proton NMR of Fe(II), Co(II), and Ni(II) derivatives. For three Co(II) derivatives Rouf, Mareš, and Vaara have tested theoretical and computational methods of calculating molecular properties, *e.g.*, ^{1}H pNMR parameters.[26] Clearly, pyrazolylborate derivatives of many other paramagnetic ions exist or are conceivable and, given the diversity of this chemistry, some general questions from a pNMR point of view emerge:

Which TpM-type compounds are worth investigating?
What are the most useful nuclei?
At what theoretical level can the spectra be reproduced?
Do the calculated signal shifts support the signal assignment and thus the determination of the molecular and electronic structure?
How are the signal shifts composed?

Along these lines we have studied the parent compounds (Figure 1a) Tp_2M (M = Cu, Ni, Co, Fe, Mn, Cr, and V), their monocations $[Tp_2M]^+$ (M = Fe, Cr, and V), the methylated analogues Tp^*_2M (Tp* = hydrotris(3,5-dimethylpyrazole)borate, M = Cu, Ni, Co, Fe, Mn, Cr, and V), and $[Tp^*_2M]^+$ (M = Fe, Cr, and V). The present paper reports the ^{1}H, ^{13}C, ^{11}B, and ^{14}N NMR spectral data and their theoretical interpretation. To this end, first-principles calculations according to the recently redressed version[27,28] of the Kurland-McGarvey theory[29] have been carried out. These computations provide the respective overall pNMR signal shifts and their tensorial components, as well as contributions from various physical interactions. Thus some basic theory will be outlined before describing the results arranged according to the d-electron count of the compounds. Finally, common trends of the series shall be discussed. Throughout this work the signal shifts are given in ppm at the respective measuring temperature relative to TMS (^{1}H, ^{13}C), $BF_3(OEt_2)$ (^{11}B), and $MeNO_2$ (^{14}N). Relevant NMR information and the syntheses of the compounds are described in the Supporting Information.

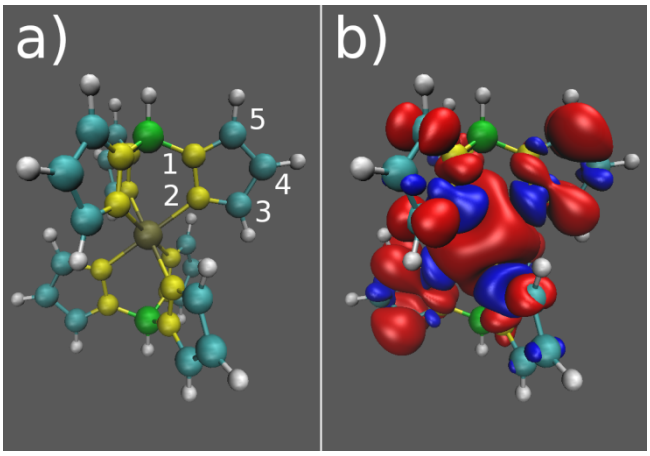

Figure 1. $[Tp_2V]^+$ a) geometry with numbering used for NMR signal assignment and b) calculated spin density isosurfaces with the isovalues of -0.0002 a.u. and 0.0002 a.u. for the negative (blue) and positive (red) surfaces, respectively. In the Tp^*_2M complexes, methyl groups replace hydrogens in positions 3 and 5.

THEORETICAL AND COMPUTATIONAL BACKGROUND

The calculation of pNMR shieldings is based on the Kurland-McGarvey theory,[29] which utilizes the ground multiplet with $2S+1$ states (S is the electron spin quantum number), parametrized by the electron paramagnetic resonance (EPR) Hamiltonian. The theory was presented in its correct form in the modern context by Soncini and Van den Heuvel,[27] and analyzed using the thermal occupations of the ground multiplet states and "magnetic couplings" between non-degenerate states by Vaara, Rouf and Mareš,[28] leading to the following formula for the Cartesian $\varepsilon\tau$-component of the pNMR shielding tensor for nucleus K:

$$\sigma_{K,\varepsilon\tau} = \sigma^{\mathrm{orb}}_{K,\varepsilon\tau} - \frac{\mu_B}{\gamma_K \hbar k T} \sum_{ab} g_{\varepsilon a} \langle S_a S_b \rangle A_{K,b\tau}, \tag{1}$$

where $\sigma^{\mathrm{orb}}_{K,\varepsilon\tau}$, γ_K and $A_{K,b\tau}$ are the Cartesian component of the orbital shielding tensor, the gyromagnetic ratio and the component of the hyperfine coupling (HFC) tensor describing the interaction between the unpaired electron spin and the spin of the nucleus K, respectively; $g_{\varepsilon a}$ is the component of the g-tensor parametrizing the interaction of the unpaired electron with the external magnetic field. The quantities μ_B, k and T are the Bohr magneton, Boltzmann constant and absolute temperature, respectively. The dyadic $\langle \boldsymbol{SS} \rangle$ results from the effective spin operator $\boldsymbol{S}$ as

$$\langle S_a S_b \rangle = \frac{\sum_{nm} Q_{nm} \langle n|S_a|m\rangle\langle m|S_b|n\rangle}{\sum_n \exp\left(-E_n/kT\right)}. \tag{2}$$

Here, Q_{nm} are elements of a symmetric matrix

$$Q_{nm} = \begin{cases} \exp(-E_n/kT), & E_n = E_m \\ -\dfrac{kT}{E_m - E_n}[\exp(-E_m/kT) - \exp(-E_n/kT)], & E_n \neq E_m \end{cases}, \quad (3)$$

and $|n\rangle$, E_n are the eigenfunctions and eigenvalues of the zero-field splitting (ZFS, non-vanishing only for $S \geq 1$) Hamiltonian $\boldsymbol{S} \cdot \boldsymbol{D} \cdot \boldsymbol{S}$ at the limit of a vanishing external magnetic field, $\boldsymbol{D}$ being the ZFS tensor.

Excited multiplets may be included to a limited extent by using the electronic wavefunctions and the magnetic operators coupling them directly instead of parametrizing the problem using the EPR Hamiltonian.[30] This approach is not yet routinely applicable, however.

The HFC tensor can be decomposed as[31,32]

$$\boldsymbol{A} = A_{\mathrm{con}}\mathbf{1} + \boldsymbol{A}_{\mathrm{dip}} + A_{\mathrm{pc}}\mathbf{1} + \boldsymbol{A}_{\mathrm{dip,2}} + \boldsymbol{A}_{\mathrm{as}}, \quad (4)$$

where A_{con} and $\boldsymbol{A}_{\mathrm{dip}}$ are the nonrelativistic isotropic contact coupling and anisotropic dipolar coupling tensors, A_{pc} is the isotropic pseudocontact coupling,[33] $\boldsymbol{A}_{\mathrm{dip,2}}$ is the anisotropic and symmetric second dipolar term, $\boldsymbol{A}_{\mathrm{as}}$ is the antisymmetric term and $\mathbf{1}$ is a 3×3 unit matrix. These three last contributions arise from relativistic influences on HFC, obtained either using perturbation theory[33] or by fully relativistic calculation.[34] Similarly, the *g*-tensor can be decomposed as[31]

$$\boldsymbol{g} = g_{\mathrm{e}}\mathbf{1} + \Delta g_{\mathrm{iso}}\mathbf{1} + \Delta\tilde{\boldsymbol{g}}, \quad (5)$$

where g_{e} is the free-electron *g*-factor, whereas Δg_{iso} and $\Delta\tilde{\boldsymbol{g}}$ are the isotropic and anisotropic parts of the *g*-shift tensor, respectively.

The chemical shift of the nucleus K, δ_K, is expressed as the difference between the isotropic pNMR shielding constant of the nucleus σ_K,

$$\sigma_K = \frac{\sigma_{K,xx} + \sigma_{K,yy} + \sigma_{K,zz}}{3}, \quad (6)$$

where $\sigma_{K,\varepsilon\varepsilon}$ are the diagonal components of the tensor $\boldsymbol{\sigma}_K$, and the shielding constant of the same isotope in a diamagnetic reference molecule, σ_{ref}:

$$\delta_K = \sigma_{\mathrm{ref}} - \sigma_K. \quad (7)$$

By electronic structure calculations and the decompositions of $\boldsymbol{A}$ and $\boldsymbol{g}$ in Eqs. (4—5), the isotropic shielding constant can be broken down to its physical contributions. Up to order $\mathcal{O}(\alpha^4)$ in the fine structure constant α, the contributions are

$$\sigma = \sigma_{\mathrm{orb}} + \sigma_{\mathrm{con}}(1) + \sigma_{\mathrm{con,2}}(3) + \sigma_{\mathrm{con,3}}(6) + \sigma_{\mathrm{dip}}(2) + \sigma_{\mathrm{dip,2}}(4) + \sigma_{\mathrm{dip,3}}(7) + \sigma_{\mathrm{c,aniso}}(8) + \sigma_{\mathrm{pc}}(9). \quad (8)$$

The detailed breakdown of the various contributions to the total nuclear shielding is given in the Supporting Information (Table SI1). The numbers given in parentheses in Eq. (8) refer to the hyperfine terms given in that table and will be used in the discussion of the present results. In particular, the first term in Eq. (8), σ_{orb}, is referred to as the "chemical shift" term in the NMR literature and the leading term 1 (σ_{con}) in the remaining, hyperfine shielding expansion in (8) is dictated by spin density; see the plot in Figure 1b) for $[Tp_2V]^+$. It should be noted in this context that the spin density at the nuclei cannot be assessed reliably from such plots, which better serve in illustrating the spatial symmetry and extent of the spin-density distribution. In addition, the different physical contributions to the calculated shielding constants of each Tp_2M and Tp^*_2M complex are listed in the SI.

The geometry optimization of the systems was carried out with the TURBOMOLE software[35] using the unrestricted Kohn-Sham DFT method with the PBE0 functional,[36] the DFT-D3 BJ dispersion correction[37,38] and the def2-TZVP basis set[39] on light atoms. For the metal center, the Stuttgart-type scalar relativistic effective core potential ECP10MDF[40] was used, along with the appropriate 6s5p3d2f1g/8s7p6d2f1g (in the contracted/uncontracted notation) valence basis set. The optimized geometries are given in the Supporting Information (Tables SI2-SI22).

The EPR parameters $\boldsymbol{g}$, $\boldsymbol{D}$ and $\boldsymbol{A}$ were calculated using a previously developed, efficient "modus operandi".[26,34] The g- and the critical $\boldsymbol{D}$ tensors were calculated at the ab initio NEVPT2 level,[41,42,43] based on a state-averaged CASSCF[44] wavefunction correlating *n* electrons of the metal with the configuration d^n in the five metal 3d-orbitals [CAS(*n*,5)]. In these calculations, the DKH-def2-TZVP basis set[45] was used on the metal and the atoms directly bonded to it, and the DKH-def2-SVP basis set on other atoms. This kind of locally dense basis has proven to save computational resources without sacrificing much accuracy. The Douglas-Kroll-Hess method (DKH2)[46] was used to approximate scalar relativistic effects, and spin-orbit effects (including the picture-changed spin-orbit operator) were calculated with the quasidegenerate perturbation theory (QDPT) method.[47] Only the spin-orbit contribution to the zero-field splitting was considered. The spin-spin contribution was determined to be small in comparison (see the Supporting Information, Table SI23). The computations of $\boldsymbol{g}$ and $\boldsymbol{D}$ were carried out with the ORCA program package.[48]

Calculating the $\boldsymbol{A}$-tensor reasonably requires considering the spin polarization of the core electrons. Therefore, the unrestricted DFT-based, fully relativistic four-component matrix Dirac-Kohn-Sham (mDKS) method[49] was employed using the full, uncontracted DKH-def2-TZVP basis set on the light atoms and the uncontracted Dyall-VTZ basis set[50] on the metal atom. This method includes both scalar relativistic and spin-orbit effects variationally. Of importance is the choice of the exchange-correlation functional, which can have a significant effect on the computed HFC. Here, the hybrid functional PBE0[36] with 25 percent exact Hartree-Fock exchange admixture was used. Another reasonable choice has been the PBE-40 functional,

which includes 40 percent exact exchange.[51] The ReSpect program[52] was used in the HFC calculations. By using the fully relativistic method for HFC we do not get the distinct nonrelativistic and relativistic contributions to the contact and dipolar HFC, in Eq. (4). Instead, the analysis of paramagnetic shifts has to be based on the rank-0, -2, and -1 contributions to the HFC tensor, corresponding to the isotropic hyperfine coupling constant, the anisotropic but symmetric part of $\boldsymbol{A}$, and the anisotropic and antisymmetric part, respectively. Hence, in Eq. (8), the con and con,2, as well as the dip and dip,2 tensors appear together. Particularly from the point of view of variational, infinite-order treatment of relativistic effects on HFC, we do not strictly limit ourselves to the $\mathcal{O}(\alpha^4)$ terms in the shielding results presently.

The orbital shielding term σ_{orb} is less critical than $\boldsymbol{g}$, $\boldsymbol{D}$ and $\boldsymbol{A}$, and this contribution was computed with the unrestricted Kohn-Sham DFT method, PBE0 functional, and the DKH-def2-TZVP basis set, using the Gaussian 09 software.[53]

The shielding constants of the closed-shell reference compounds, σ_{ref} in Eq. (7), were calculated at the corresponding PBE0/DKH-def2-TZVP level of theory as the orbital shielding term for the transition metal complexes, with the Gaussian 09 program. The computed reference shieldings are tabulated in the Supporting Information (Table SI24).

We discuss three of the central methodological choices in the present study, the choice of the exact exchange admixture in our PBE-based hybrid DFT functional, omission of solvent effects, and limiting the study solely to the ground multiplet. Tests of these choices were performed for one of the most challenging present systems, $[Tp_2Fe]^+$, and their results will be assessed below in connection with this system.

The results are compiled for all the present systems in the Supporting Information, Tables SI25-SI27, in addition to the discussion below.

RESULTS AND DISCUSSION

d^9, Tp_2Cu, Tp^*_2Cu, S = 1/2. The proton NMR spectrum of Tp^*_2Cu (Figure 2) shows signals which can be assigned according to the signal widths. For molecules with considerable magnetic anisotropy and short distances between the metal and the ligand nuclei (as in this work), through-space or dipolar nuclear relaxation is a major contribution to the signal half width $\Delta\nu_{1/2}$. Hence, as a reasonable approximation, $\Delta\nu_{1/2} \propto 1/r^6$ where r is the distance between the observed nucleus and the spin center, here the copper atom.[25,54] A comprehensive overview of the various relaxation sources (and pNMR in general) has recently been published by Pell *et al*.[55] More details relevant for the present work are given in the Supporting Information including the measured signal widths of all compounds (Table SI34). The distance sequence Cu-Me3 < Cu-Me5 (see Table SI33) entails $\Delta\nu_{1/2}$(Me3) > $\Delta\nu_{1/2}$(Me5) and

leads to the assignment in Figure 2, while H4 appears in the same signal shift range as H4 of Tp_2Cu.

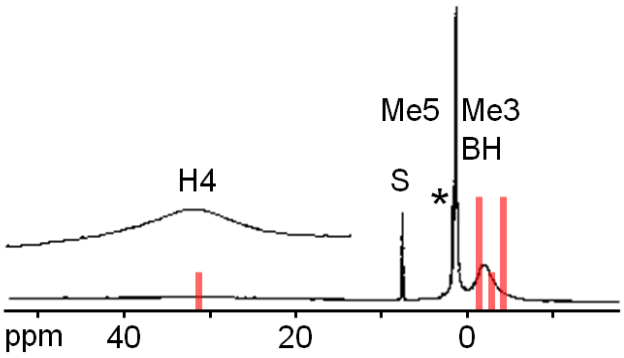

Figure 2. ^{1}H NMR spectrum of Tp^*_2Cu in $CDCl_3$ at 305 K. The calculated signal shifts are shown as red bars, from left: H4, Me5, BH, Me3. S = residual solvent protons, * = impurity.

The proton spectrum of Tp_2Cu (Figure SI2) suggests that the BH signal of Tp^*_2Cu coincides with that of Me3. The signal assignments agree with the calculated shifts in Table 1. In particular, the latter confirm the position of the BH signals and that the pyrazole signals H3, H4, and H5 all have positive shifts. H3 and H5 can be distinguished based on the calculated shifts. It turns out that the theoretical pNMR shifts are an important support for the study of TpCu(II) derivatives which do show ^{1}H NMR signals unlike suspected previously.[23]

Table 1. Signal Shifts of Tp_2Cu and Tp^*_2Cu.

Nuclear position	3	Me3	4	5	Me5	BH
			Tp_2Cu			
δ^{exptl} (^{1}H)[a]	29		23	29		−3.4
δ^{calcd} (^{1}H)[a]	31.3		29.3	33.8		−2.4
δ^{calcd} (^{13}C)[b]	405.0		387.8	456.4		
other shifts	δ^{exptl} (^{11}B)[b] = −24.3; δ^{calcd} (^{11}B)[b] = −22.9 δ^{exptl} (^{14}N1) = [c] ; δ^{calcd} (^{14}N1)[b] = 337.4					
			Tp^*_2Cu			
δ^{exptl} (^{1}H)[a]		−2.3	32		1.0	−2.3
δ^{calcd} (^{1}H)[a]		−4.1	31.6		−1.3	−2.7
δ^{exptl} (^{13}C)[d]	[c]	32.0	[c]	[c]	16.0	
δ^{calcd} (^{13}C)[d]	374.7	28.4	341.4	365.9	39.7	
other shifts	δ^{exptl} (^{11}B)[b] = −28.9; δ^{calcd} (^{11}B)[b] = −31.1 δ^{exptl} (^{14}N1) = [e] ; δ^{calcd} (^{14}N1)[b] = 294.6					

[a] 305 K. [b] 298 K. [c] Not observed. [d] 398 K. [e] Not measured.

Attempts to detect ^{13}C NMR signals of Tp_2Cu and Tp^*_2Cu at room temperature failed. After increasing the temperature and thus slowing down the nuclear relaxation rate the signals of Me3 and Me5 were found (Figure SI3) while those of C3, C4, and C5 could not be detected in an extended shift range. The calculations confirm the experimental signal shift range of Me3 and Me5 while the assignment is different from that suggested by the respective signal widths.

As for ^{11}B NMR, there is good agreement between the calculated and experimental shifts; for Tp_2Cu Jesson *et al.*[22,23] have reported a similar value (−26.3 ppm).

In these doublet systems the computationally challenging ZFS interaction does not occur. The *g*-tensor is quite anisotropic and deviates a lot from the free-electron *g*-factor in one of its principal components, indicating appreciable spin-orbit interaction. Our data (Table SI23 in SI) confirm the EPR measurements of Tp_2Cu[56,57] and Tp^*_2Cu[58] in solid solution. Overall, the calculated shifts agree well with the experimental ones, being mostly slightly larger in absolute value. Ring protons 4 and

5 have exaggerated computed shifts by 5-6 ppm, in addition to the inverted assignment of Me3 and Me5 ^{13}C signals, as mentioned above.

The hyperfine part of the total shieldings of Tp_2Cu and Tp^*_2Cu is dominated primarily by the nonrelativistic contact term 1, with smaller contributions by the “con,3” term (term number 6) arising from *g*-tensor anisotropy and isotropic hyperfine coupling (see Tables SI28-SI30 in SI). The other physical contributions are negligible, apart from the slightly non-zero pseudocontact term. The orbital contributions are important throughout all the calculated signals, although they cancel effectively with the contact shift (term 1) in the special case of ring protons 3, 4 and 5.

d^8, Tp_2Ni, Tp^*_2Ni, *S* = 1. In early reports on Tp_2Ni the signals of H3-H5 were not resolved[22,23] while for Tp^*_2Ni the BH signal was missing.[23,59] Now Tp_2Ni shows the expected four signals (Figure SI4) and the comparison with Tp^*_2Ni (Figure SI5) suggests that the BH signal of Tp^*_2Ni coincides with the signal of Me3. This conclusion is ensured by the theory and, generally, the experimental proton shifts are well reproduced (Table 2) except for the sequence of the closely shifted signals of H4/5.

Table 2. Signal Shifts of Tp_2Ni and Tp^*_2Ni.

Nuclear position	3	Me3	4	5	Me5	BH
			Tp_2Ni			
δ^{exptl} (^{1}H)[a]	39.8		48.2	50.3		−8.8
δ^{calcd} (^{1}H)[a]	56.2		48.1	54.8		−8.0
δ^{exptl} (^{13}C)[b]	683		558	653		
δ^{calcd} (^{13}C)[b]	599.1		593.5	662.5		
other shifts	δ^{exptl} (^{11}B)[c] = −34.2; δ^{calcd} (^{11}B)[c] = −25.2 δ^{exptl} (^{14}N1)[c] = 559; δ^{calcd} (^{14}N1)[c] = 507.5					
			Tp^*_2Ni			
δ^{exptl} (^{1}H)[d]		−9.0	50.8		−2.1	−9.0
δ^{calcd} (^{1}H)[d]		−16.7	47.7		−5.6	−15.2
δ^{exptl} (^{13}C)[e]	566	0.3	462	462	31.1	
δ^{calcd} (^{13}C)[e]	509.1	20.2	506.4	470.6	49.4	
other shifts	δ^{exptl} (^{11}B)[c] = −36.1; δ^{calcd} (^{11}B)[c] = −62.8 δ^{exptl} (^{14}N1) = [f] ; δ^{calcd} (^{14}N1)[c] = 311.1					

[a] 305 K. [b] 332 K. [c] 298 K. [d] 303 K. [e] 385 K. [f] Not measured.

The ^{13}C NMR signals of C3-C5 of both compounds are strongly shifted to high frequency (Figures 3 and SI6), those of Me3/5 far less. The signal assignment given in Table 2 is suggested by the signal widths. In Figure 3 the signal of Me5 is hidden under the methyl signal of the solvent anisole while in benzene at ambient temperature it appears as isolated quartet. Under the latter conditions the signals of C3-5 merge into the baseline.

The theory reproduces the ^{1}H and ^{13}C signal shift ranges rather well. It is noteworthy that, similarly to the Me3/5 signals in Tp^*_2Cu, the calculations favor the opposite assignment for both H3/5 and C3/5, as compared to what is assigned by the line widths of Tp_2Ni.

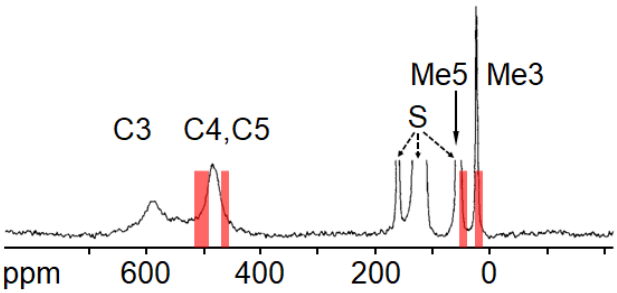

Figure 3. ^{13}C NMR spectrum of Tp*$_2$Ni in anisole at 385 K. The calculated signal shifts are shown as red bars, from left: C3, C4, C5, Me5, Me3. S = solvent signals.

The calculated ^{11}B NMR signal shifts of Tp$_2$Ni and Tp*$_2$Ni are again in accord with the experimental ones and for Tp$_2$Ni the published value (–36.0 ppm)[22,23] is confirmed. In the ^{14}N NMR spectrum of Tp$_2$Ni the only signal observed was assigned to N1. Throughout this study N2 was never detected. Actually, since N2 is the ligand atom closest to the metal its signal is expected to be broadened beyond the detection limit. The calculated shifts of N2 are in the range –11000 ppm to 23000 ppm (Table SI27) which would be an experimental challenge.

The large signal widths of the spectra (Table SI34) are a consequence of the rather long electron relaxation times of Ni^{2+} ions[25,54,55] which, in turn, suggests complementary EPR studies. However, this type of compounds exhibits zero-field splittings that prevent routine EPR work[60] and, to our knowledge, the EPR spectra of Tp$_2$Ni and Tp*$_2$Ni have not been published so far.

The *S*=1 Ni^{2+} systems feature ZFS with rather small *D*-parameters equal to -0.4 and -2.2 cm^{-1} for Tp$_2$Ni and Tp*$_2$Ni, respectively (Table SI23), rendering the ZFS effects on chemical shifts rather small. These systems also feature a rather isotropic *g*-tensor with eigenvalues around 2.17-2.19. Our *D* and *g* values confirm those found for Tp*NiL derivatives (L=Cl, Br,[61] and BH_4[62]) Similarly to the Cu-systems, an overall satisfactory, albeit non-quantitative agreement with experimental signals is found. The lack of quantitative match with experiment may be due to various model parameters including the DFT functional used for HFCs, as well as using a static *in vacuo* model for the calculation.

As with the Cu complexes, the hyperfine shieldings of Tp$_2$Ni and Tp*$_2$Ni are dominated by the nonrelativistic contact term 1, with smaller contributions by the “con,3” term 6 (Tables SI28-SI30). Due to the presence of small ZFS, the isotropic shielding due to the dipolar interaction (term 2) is non-vanishing, albeit small. The comparatively isotropic *g*-tensor renders the pseudocontact term 9 small in comparison to the Cu systems. The orbital shieldings of corresponding nuclei in Tp$_2$Ni and Tp*$_2$Ni are rather different, which implies that there are significant orbital shift contributions and that the concept of “equivalent diamagnetic complex” (whose

orbital shieldings would be used to eliminate orbital contributions to pNMR shifts) may not be applicable.[63]

d^7, Tp_2Co, Tp^*_2Co, *S* = 3/2. The proton relaxation times of Tp_2Co and Tp^*_2Co are shortened by a dynamic Jahn-Teller effect[64] favoring well-resolved spectra as can be seen in Figures 4, SI7, SI8, and SI9. Accordingly, the ^1H NMR spectra of TpCo(II)-type compounds are being recorded routinely since the first reports.[22,23] The data listed in Table 3 show good agreement between theoretical and measured signal shifts. We have previously calculated the proton data of Tp_2Co;[26] since then the calculations have been improved[34] by incorporating scalar relativistic effects into the computation of ***g*** and ***D*** by ORCA, as well as by adopting the fully relativistic mDKS method for the ***A***-tensors in the ReSpect code. A bookkeeping error bearing on the signal assignment[26] has been noted and corrected in Ref.[34] and presently.

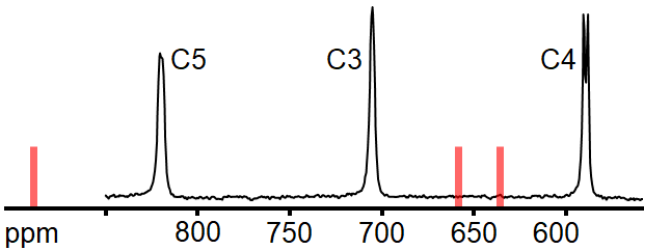

Figure 4. ^{13}C NMR spectrum of Tp_2Co in anisole at 298 K, expanded range. The calculated signal shifts are shown as red bars, from left: C5, C4, C3.

Table 3. Signal Shifts of Tp_2Co and Tp^*_2Co.

Nuclear position	3	Me3	4	5	Me5	BH
			Tp_2Co			
δ^{exptl} (^{1}H)[a]	−105.3		40.9	91.0		116.9
δ^{calcd} (^{1}H)[a]	−93.9		38.7	97.4		129.1
δ^{exptl} (^{13}C)[b]	705		589[c]	820[d]		
δ^{calcd} (^{13}C)[b]	636.2		659.0	889.6		
other shifts	δ^{exptl} (^{11}B)[b] = 280; δ^{calcd} (^{11}B)[b] = 310.8 δ^{exptl} (^{14}N1)[b] = 602; δ^{calcd} (^{14}N1)[b] = 617.9					
			Tp^*_2Co			
δ^{exptl} (^{1}H)[a]		−76.4	44.1		41.8	105.5
δ^{calcd} (^{1}H)[a]		−80.4	45.7		41.4	112.6
δ^{exptl} (^{13}C)[a]	782	−99.0	608	782	86.3	
δ^{calcd} (^{13}C)[a]	758.4	−76.1	695.1	817.8	99.9	
other shifts	δ^{exptl} (^{11}B)[b] = 280; δ^{calcd} (^{11}B)[b] = 271.1 δ^{exptl} (^{14}N1) [e] ; δ^{calcd} (^{14}N1)[b] = 448.0					

[a] 305 K. [b] 298 K. [c] ^1J(C,H) = 171 ± 5 Hz. [d] ^1J(C,H) = 180 ± 5 Hz. [e] Signal could not be localized in an extended range.

The ^{13}C NMR signals of Tp_2Co (Figure 4) are remarkably narrow as well and show the ^1J(C,H) coupling of C4 while it is hardly resolved for C5 and quenched for C3. This sequence is expected when the nuclear relaxation is determined by the metal-nuclear distances and assures the signal assignment (see SI). No such couplings could be observed for Tp^*_2Co. Here the signals of C3-5 are identified by the signal shifts that are similar to the calculated shifts and to those of Tp_2Co (Table 3). The unique criterion for distinguishing the signals of Me3/5 are the theoretical signal shifts. In general, the theoretical and experimental signal shifts are in accord. An exception is the theoretical signal sequence of C3 and C4 of Tp_2Co which is opposed to what the experimental signal widths suggest. The approximations of the computational model (*vide infra*) can easily produce uncertainty of the present size to the computed shifts, however.

Aubagnac *et al.*[65] have reported somewhat different ^{13}C NMR data.[66] Their signal assignment has not been explained and is at variance with that in Table 3. The calculated ^{11}B NMR data are close to the measured ones while for Tp_2Co Jesson has reported 254 ppm. [22,23]

Tierney *et al*.[67] have determined A_{iso}(H3), A_{iso}(BH) and A_{iso}(N2) using Q- and X-band ENDOR spectroscopy (Table SI31). Our computed, large mDKS hyperfine coupling for the last nucleus agrees very well with the experiment (Table SI31).

These S = 3/2 cobalt systems feature large spin-orbit coupling effects, manifested by the calculated D-parameter of ZFS equal to -110 and -102 cm^{-1} for Tp_2Co and Tp^*_2Co, respectively, as well as the very anisotropic g-tensor with eigenvalues deviating substantially from the free-electron g-factor (Table SI23). Calculation of shifts without considering ZFS would be effectively meaningless for these systems.[26] Tierney *et al*.[68] determined the zero-field splitting from EPR relaxation and obtained $|D|$ ~ 10 cm^{-1}. Krzystek *et al*. found similar values using HFEPR spectroscopy for the S = 3/2 complex $Co(PPh_3)_2Cl_2$[69] (D = -14.7 cm^{-1}; E = 1.14 cm^{-1}) and for a TpCo derivative[70] (D = 7.46 cm^{-1}; E = 1.58 cm^{-1}). The recent THz-EPR experiments by Pavlov *et al*.[71] put the D-parameter much closer to our present data, at -98.5 cm^{-1}. As previously discussed,[72] our computational method can overestimate the zero-field splitting in Co(II) systems. The NMR experiments and corresponding theoretical calculations are performed at around the room temperature, whereas EPR data are typically taken at very low temperatures, Regardless of the discrepancies with existing EPR data on related systems, the calculated pNMR shifts are even more sensitive to the quality of the hyperfine couplings than to that of the ***D***-tensor, which diminishes the influence of the latter on the results.

The breakdown of physical contributions to the pNMR shieldings of Tp_2Co and Tp^*_2Co varies with the nuclear position. However, the contact, dipolar, and pseudocontact terms 1, 2 and 9 are often the most significant contributors, especially for the proton and ^{11}B shieldings (Tables SI28-SI30). The dipolar term contributes large isotropic shifts solely due to the large ZFS (the “dip” shift term vanishes for doublet systems). The large pseudocontact term is due to the strong and anisotropic g-shift.

d^6, Tp_2Fe, Tp^*_2Fe, S = 0 ⇌ 2. We begin with Tp^*_2Fe, which is a S = 2 compound at room temperature and whose ^{1}H and ^{13}C NMR signal shifts are much larger than those of Tp_2Fe (Figures 5 and SI11, Table 4).

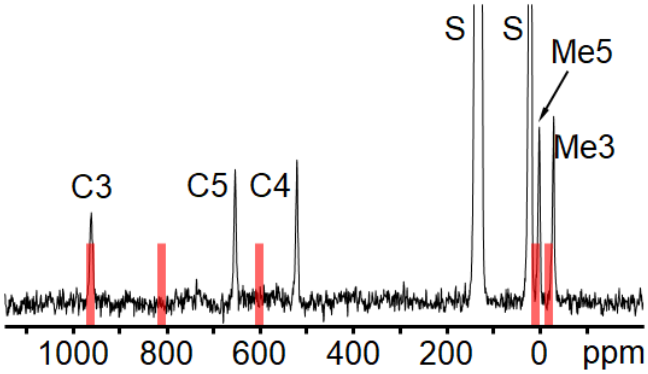

Figure 5 ^{13}C NMR spectrum of Tp*$_2$Fe in toluene at 298 K. The calculated signal shifts are shown as red bars, from left: C3, C5, C4, Me5, Me3. S = solvent signals.

The assignment of the ^{1}H and ^{13}C signals in Tp*$_2$Fe follows the trend of their half widths (Supporting Information) and complements previous proton NMR data of Tp$_2$Fe.[24] In the sequence C3, C5, C4 the signals become so narrow that C4 and C5 show one-bond C,H coupling (Figure SI12). The signal sequences are exactly predicted by the theory and the computed shift values are close to the experimental ones (Table 4).

On the other hand, Tp$_2$Fe undergoes spin crossover observable near ambient temperature, and this has first been studied by Jesson *et al*. using ^{1}H NMR spectroscopy.[24] In the context of the theoretical shifts we have repeated this work. The ^{1}H (Figure SI10) and ^{13}C NMR (Figure SI12) spectra near room temperature show the mean signals of rapid spin interconversion.

Table 4. Signal Shifts of Tp_2Fe and Tp^*_2Fe.

Nuclear position	3	Me3	4	5	Me5	BH
			Tp_2Fe			
δ^{exptl} (^{1}H)[a]	13.0		12.9	8.1		–2.7
δ^{calcd} (^{1}H)[a]	16.8		17.2	9.3		–3.4
δ^{exptl} (^{13}C)[b]	266		168[c]	229[d]		
δ^{calcd} (^{13}C)[b]	364.3		246.7	355.7		
other shifts	δ^{exptl} (^{11}B)[c] = –26.4; δ^{calcd} (^{11}B)[c] = –41.7 δ^{exptl} (^{14}N1)[c] = –126; δ^{calcd} (^{14}N1)[c] = –144.4					
			Tp^*_2Fe			
δ^{exptl} (^{1}H)[b]		39.0	47.5		12.8	-42.5
δ^{calcd} (^{1}H)[b]		37.2	53.0		19.5	-33.8
δ^{exptl} (^{13}C)[e]	961	–30.0	520	652	0.9	
δ^{calcd} (^{13}C)[e]	963.9	–19.6	601.1	809.7	9.0	
other shifts	δ^{exptl} (^{11}B)[e] = –138; δ^{calcd} (^{11}B)[e] = –118.9 δ^{exptl} (^{14}N1) = [f] ; δ^{calcd} (^{14}N1)[e] = –288.0					

[a] 290 K. [b] 305 K. [c] ^1J(C,H) = 171 ± 3 Hz. [d] ^1J(C,H) = 186 ± 3 Hz. [e] 298 K. [f] Signal could not be localized in an extended range.

The temperature series of the Tp_2Fe proton shifts was calculated theoretically for the pure S = 2 state and measured experimentally (Figure 6). The theoretical predictions do not agree with experiment even qualitatively, apart from H5. Better compatibility with measurements was achieved through considering the high-spin/low-spin (HS/LS) equilibrium obtained by fitting the enthalpy gap $\Delta H = H_2 - H_0$ and the entropy gap $\Delta S = S_2 - S_0$ between the diamagnetic (S = 0) and paramagnetic (S = 2) states in a Boltzmann-weighted mixture, using the least-squares method. With the inclusion of entropy, the Boltzmann factor of the state i assumes the form

$$p_i = \frac{1}{Z} e^{-\frac{H_i}{kT} + \frac{S_i}{k}}, \tag{9}$$

where $Z = \sum_i e^{-\frac{H_i}{kT}+\frac{S_i}{k}}$ is the partition function and H and S_i are the enthalpy and entropy of the states involved in the spin transition. The present shielding calculations for both HS and LS states were fitted to the experimental temperature dependence of the ^{1}H chemical shifts in Tp_2Fe. The fitted parameters ΔH and ΔS obtained the values 21.1 kJ/mol and 63.0 J/(K mol), respectively, and are in fairly good agreement with the experimental values of 16.1 kJ/mol and 47.7 J/(K mol) obtained from temperature-dependent measurements of the magnetic susceptibility in solution.[24]

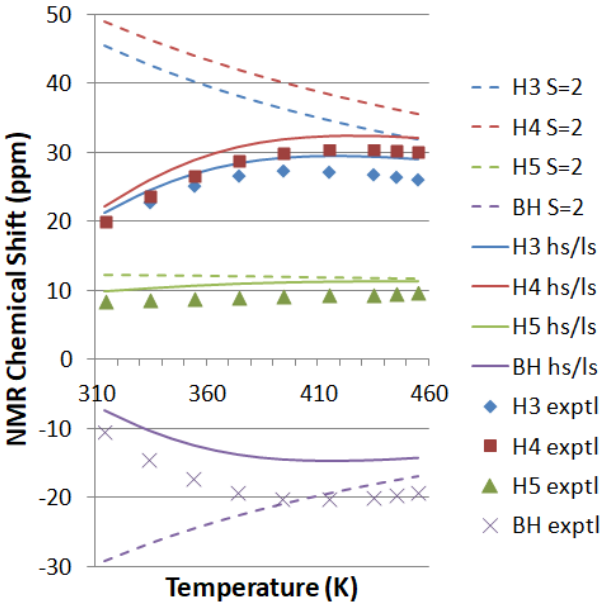

Figure 6. Proton chemical shifts of Tp_2Fe in the pure paramagnetic (S = 2, hs) state (dashed lines) and in a fitted, Boltzmann-weighted high-spin/low-spin equilibrium state (solid lines, hs/ls), along with the corresponding experimentally measured signal shifts.

The parameters ΔH and ΔS can alternatively be fitted for each equivalent group of nuclei separately, as opposed to a joint fit discussed above. This approach resulted in an improved match of the calculated shifts with experiment as compared to the joint fit illustrated in Figure 6, and fit parameters in the range of 15.6 – 39.2 kJ/mol and 45.3 – 122.3 J/(K mol) for ΔH and ΔS, respectively.

The spin equilibrium has also been analyzed by the classical approach (for details see the Supporting Information) using

$$\delta_{K,\mathrm{iso}}^{\mathrm{con}} = \frac{2 g_{\mathrm{iso}} \beta_{\mathrm{e}}}{\gamma_K kT} A_{\mathrm{iso}} \left[\exp\left(\frac{\Delta H}{RT} - \frac{\Delta S}{R}\right) + 1\right]^{-1}, \qquad (10)$$

where g_{iso} is the mean of the g-factor components, β_{e} is the Bohr magneton, A_{iso} is the isotropic hyperfine coupling constant, and R is the universal gas constant. The temperature-dependent signal shifts of H4, which are least affected by through-space

interaction, yield ΔH = 24 kJ mol^{-1} and ΔS = 70 J mol^{-1} K^{-1} in good agreement with the theoretical result above.

The S = 2 Tp_2Fe and Tp^*_2Fe systems are characterized by appreciable spin-orbit coupling effects, as evidenced by the D-parameter of ZFS around 9 cm^{-1} and the g-tensor eigenvalues deviating significantly from the free-electron g-factor (Table SI23). Experimental confirmation must await high-field EPR spectra, for instance, but similar values have been found for $Fe(SO)_4(H_2O)_4$.[70] The g-anisotropy is also noteworthy. All these aspects are less pronounced in these Fe(II) compounds than in the corresponding cobalt complexes, however. These features are reflected in the significant contribution to the ^{1}H shielding constants by the dipolar shift (term 2, Tables SI28-SI30) and the "pc" term 9, which are dependent on the size of ZFS and g-tensor anisotropy, respectively. In the case of ^{13}C shieldings, the leading contact term dominates despite the dip, pc and con,3 (terms 2, 9 and 6, respectively) contributions, where the last one stems from isotropic g-shift and contact hyperfine coupling.

d^5, $[Tp_2Fe]^+$, $[Tp^*_2Fe]^+$, S = 1/2. The proton NMR spectra (Figures 7 and SI13) of both ions are well reproduced by the calculations (Table 5). Notably, they confirm the BH signal of $[Tp^*_2Fe]^+[B(C_6H_5)_4]^-$ appearing only as a low-frequency shoulder of the Me5 signal (Figure SI13). The signals of Me3 and Me5 have the same widths and had therefore to be assigned according to the calculated signal shifts. The ^{13}C signal widths of $[Tp_2Fe]^+$ show the same trend as Tp_2Fe with the nuclear relaxation being more favorable for $[Tp_2Fe]^+$. Thus ^1J(C,H) of C4 and C5 is again visible.

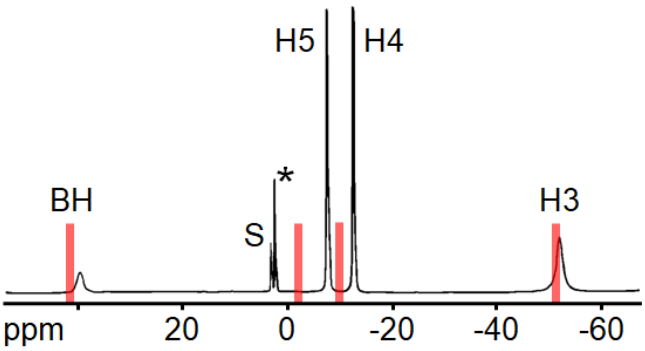

Figure 7 ^{1}H NMR spectrum of $[Tp_2Fe]^+[PF_6]^-$ in acetone-d_6 at 305 K. The calculated signal shifts of $[Tp_2Fe]^+$ are shown as red bars, from left: BH, H5, H4, H3. S = residual solvent protons, * = impurity.

Table 5. Signal Shifts of $[Tp_2Fe]^+[PF_6]^-$, $[Tp^*_2Fe]^+[B(C_6H_5)_4]^-$, and $[Tp^*_2Fe]^+[PF_6]^-$.

Nuclear position	3	Me3	4	5	Me5	BH
			$[Tp_2Fe]^+$			
δ^{exptl} (^{1}H)[a,b]	–52.9		–13.2	–8.2		39.4
δ^{calcd} (^{1}H)[a]	–51.3		–10.0	–2.0		41.5
δ^{exptl} (^{13}C)[c,b]	2.5		175.8d	19.6[e]		
δ^{calcd} (^{13}C)[c]	34.7		–3.6	93.7		
other shifts	δ^{exptl} (^{11}B)[b,f] = 95.2; δ^{calcd} (^{11}B)[f] = 91.2 δ^{exptl} (^{14}N1) = [g] ; δ^{calcd} (^{14}N1)[f] = –419.5					
			$[Tp^*_2Fe]^+$			
δ^{exptl} (^{1}H)[a,h]		3.2	–11.7		37.9	36.0
δ^{exptl} (^{1}H)[b,f]		5.3	–13.0		39.5	38.5
δ^{calcd} (^{1}H)[f]		4.3	–9.3		35.9	36.6
δ^{exptl} (^{13}C)[c,h]	12.3	–50.2	194.6	50.0	–34.0	
δ^{exptl} (^{13}C)[b,f]	10.9	–49.1	195.9	[i]	–33.1	
δ^{calcd} (^{13}C)[f]	86.3	–52.7	–25.6	122.2	–33.4	
other shifts	δ^{exptl} (^{11}B) = 89[b,f,h]; δ^{calcd} (^{11}B)[f] = 83.5 δ^{exptl} (^{14}N1) = [g] ; δ^{calcd} (^{14}N1)[f] = –491.6					

[a] 305 K. [b] $[PF_6]^-$ salt. [c] 300 K. [d] ^1J(C,H) = 179 ± 2 Hz. [e] ^1J(C,H) = 178 ± 2 Hz. [f] 298 K. [g] Not measured. [h] $[B(C_6H_5)_4]^-$ salt. [i] Signal hidden under the signal of the solvent CH_2Cl_2 (δ = 53.8).

The theoretical ^{13}C NMR chemical shifts of the ring carbons C3, C4 and C5 in both $[Tp_2Fe]^+$ and $[Tp^*_2Fe]^+$ correspond poorly to measured signal shifts. As stated above, the agreement of theory and experiment is good for the ^{1}H and ^{11}B nuclei, as well as for the methyl carbons (in $[Tp^*_2Fe]^+$). The disagreement could be partially remedied by a reassignment of the ring carbon signals such that the shifts of C3, C4 and C5 would correspond to nuclei C4, C5 and C3, respectively. This would bring the computed shifts to a qualitative, albeit far from quantitative agreement with

experiment, for both $[Tp_2Fe]^+$ and $[Tp^*_2Fe]^+$. Such a reassignment is not supported by experimental linewidth information, however. To investigate other possible sources of this disagreement from experiment, several tests of the model were carried out.

The HFC tensors as calculated by DFT represent a bottleneck in improving the accuracy of our predictions. To probe the potential influence of this error source, the HFCs were calculated with different proportions of exact exchange admixture in the DFT functional (0% corresponding to the pure PBE functional, 25% as appropriate to standard PBE0, 40% and 100%) for $[Tp_2Fe]^+$ chosen as the test system. As in the other calculations, the DKH-def2-TZVP basis set was employed, and the ZFS and *g*-tensor were calculated at the NEVPT2 level of theory. The ^{14}N nuclei were excluded due to lack of experimental measurements for them in this compound. The shift results are shown in Table 6 (see Table SI24 in SI for the corresponding reference shieldings with PBE, PBE-40 and PBE-100). Increasing the percentage of exact exchange admixture leads to a systematic change of the computed shifts in the range from 0% to 40%. For some signals with chemical shifts close to zero, this involves also a change of the sign of the shift. The shift range hence obtained may be considered indicative of the size of methodological error. In contrast, at 100% exact exchange the systematic trend in the shifts is broken, probably due to excessive spin contamination in this limit. Comparison with experiment indicates that for ^1H and ^{11}B, the choice of functional is not critically important: the shifts predicted at all exact exchange admixtures are well in line with measurements. While the problematic ^{13}C shifts show a larger variation, the suggested assignment pattern is not changed by results obtained within a reasonable range of exact exchange admixture (*i.e.*, excluding the 100% case). In particular, the line width-based assignment of C4 and C5 cannot be reproduced with any of the currently chosen functionals.

Table 6. Computed chemical shifts (ppm) for $[Tp_2Fe]^+$ with different proportions of exact exchange used in the DFT calculation of the HFC.

Nuclear position	H-3[a]	H-4[a]	H-5[a]	BH[a]	C-3[b]	C-4[b]	C-5[b]	B[c]
Experimental	-52.9	-13.2	-8.2	39.4	2.5	175.8	19.6	95.2
Exact exchange: 0% (PBE)	-44.4	-20.3	-3.1	37.1	-25.6	-6.6	63.0	69.6
Exact exchange: 25% (PBE0)	-51.3	-10.0	-2.0	41.5	34.7	-3.6	93.7	91.2
Exact exchange: 40% (PBE-40)	-55.8	-5.9	-3.0	43.6	79.9	-7.5	111.3	103.2
Exact exchange: 100% (PBE-100)	-65.4	18.3	-20.0	37.5	340.4	-83.6	253.1	116.2

[a] 305 K; [b] 300 K; [c] 298 K

As a second omitted model feature so far, explicit solvent molecules were included in the pNMR analysis. The ZFS and *g*-tensor were calculated at the CASSCF level of theory, and the DKH-def2-SVP basis set was used throughout due to computational limitations. Geometry optimization in the case of 12 solvent molecules was performed using the PBE functional (PBE0 was used otherwise, for structure optimization, HFCs and orbital shieldings), also to conserve computational resources. A calculation for the isolated $[Tp_2Fe]^+$ system was performed at the same level of theory and with the same basis set, given for comparison. The corresponding DKH-def2-SVP-quality reference shieldings are given in Table SI24 in SI. The results are shown in Table 7 (the optimized geometries are given in SI, Tables SI21 and SI22, and a figure is shown of each case in Figure SI1). Incorporation of explicit solvation in the computational model improves the already qualitatively good numerical agreement with experiment for the ^{1}H and ^{11}B signals. There is a minor difference (particularly for ^{1}H) between the smaller (8 solvent molecules) and larger (12) explicitly solvated model. Solvation influences shifts by up to around 10 ppm for ^{1}H, and 20-30 ppm for ^{13}C and ^{11}B, which is significant in detailed comparisons of theory and experiment in all the present systems.

Table 7. Computed chemical shifts (ppm) for $[Tp_2Fe]^+$ with explicit solvent molecules (acetone) included.

Nuclear position	H-3[a]	H-4[a]	H-5[a]	BH[a]	C-3[b]	C-4[b]	C-5[b]	B[c]
Experimental	-52.9	-13.2	-8.2	39.4	2.5	175.8	19.6	95.2
No solvent	-61.4	-10.9	4.8	49.5	4.7	-7.9	78.7	118.6
8 solvent molecules	-49.9	-8.7	-3.1	39.2	27.0	-15.7	92.9	90.5
12 solvent molecules	-50.0	-8.8	-3.3	40.0	32.1	-15.7	104.8	94.3

[a] 305 K. [b] 300 K. [c] 298 K.

As can be seen in Figure 8, the calculations involving variations of exact exchange admixture and explicit solvent molecules do not account for the discrepancy between theory and experiment for the ^{13}C signals in $[Tp_2Fe]^+$.

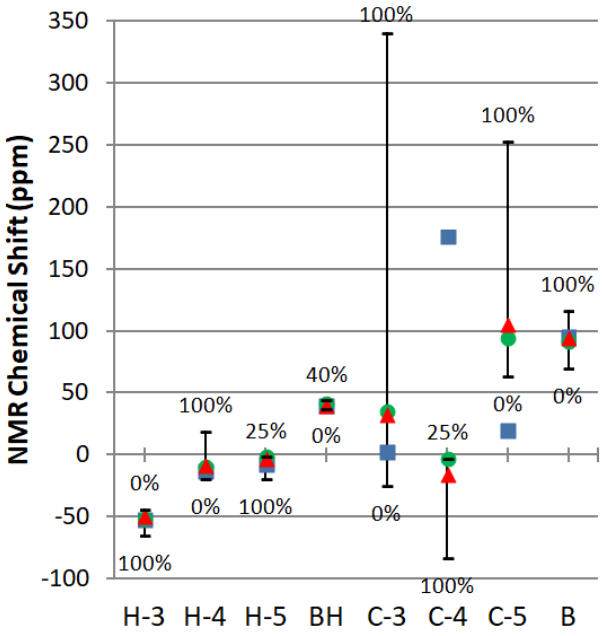

Figure 8. NMR chemical shifts calculated for $[Tp_2Fe]^+$ with and without explicit solvent molecules compared to experimental signal shifts (■). The bars represent the range of *in vacuo* results obtained with 0%, 25%, 40% and 100% exact exchange admixture in the calculation of the HFC tensor. The data points without solvent (●) and those with 12 solvent molecules (▲) are obtained with PBE0 (25% exact exchange). Calculated HFC data with the DKH-def2-TZVP basis set for *in vacuo* systems, and DKH-def2-SVP for solvated systems.

Yet another possible model deficiency is to limit the investigation to the ground multiplet only. To assess whether this can influence the present disagreement of the calculated ^{13}C shifts with experiment, a low-lying excited state 601.1 cm^{-1} above the

ground state, of the same (doublet) multiplicity as suggested by the NEVPT2 calculation, was included by computing a Boltzmann-weighted average of the calculated ground-state NMR shieldings and the shieldings assigned to this excited multiplet. The shieldings of the excited doublet were parametrized as $\sigma_{\mathrm{e,nuc}} = \sigma_{\mathrm{orb}} + C_{\mathrm{nuc}}/T$, with the orbital shieldings of the ground multiplet being used for σ_{orb} and the C_{nuc} parameters least-squares optimized for the best fit between the Boltzmann-weighted shifts and the measurements. The shieldings obtained in this way can be found in SI (Table SI32). By this *ad hoc* method, a very good numerical correspondence with experiment can be achieved. In this very approximate approach based on thermal occupations of the ground and excited doublets, the magnetic couplings[28] between the states belonging to the two doublet manifolds are omitted. The fit results in quite large shielding constants for the C3, C4 and C5 centers in the excited doublet state. We have presently no means of verifying them. However, the conclusion remains that a low-lying excited state can, at least in principle, explain the difference between theory and experiment for the ^{13}C nuclei in the $[Tp_2Fe]^+$ system.

Back to our standard first-principles calculation for the ground doublet only, the physical contributions to the pNMR shieldings of $[Tp_2Fe]^+$ and $[Tp^*_2Fe]^+$ are dominated by the contact and pseudocontact terms 1 and 9, with slight contributions from the "con,3" term 6 (Tables SI28-SI30). The specific dominant term varies with nuclear position. Both the pseudocontact and "con,3" terms obtain their significance from the large *g*-tensor anisotropy in the two systems (Table SI23).

d^5, Tp_2Mn, Tp^*_2Mn, S = 5/2. Mn^{2+} ions are known to have comparably long electron relaxation times.[54,55] Hence, near room temperature, the proton NMR spectrum of Tp_2Mn (Figure 9, bottom) shows broad signals and only three of the expected four are in evidence. The theory reliably reproduces the shift range (Table 8) and indicates that the missing signal might be hidden under the solvent signals and impurities near 2 ppm. Indeed, at 379 K a higher concentrated sample uncovers another broad signal at 3.6 ppm (Figure 9, top) or ~4.6 ppm at 298 K. The proton signals of Tp^*_2Mn are much broader than those of Tp_2Mn and they strongly overlap even at high temperature (Figure SI16). Actually, the theoretical shifts were essential for the signal assignment (Table 8).

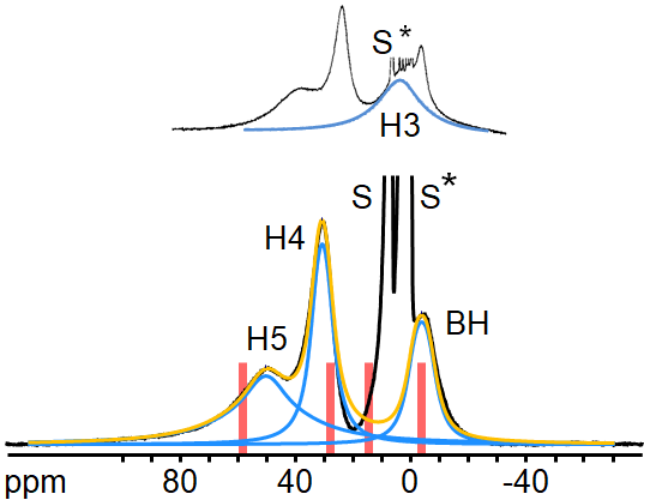

Figure 9. ^{1}H NMR spectrum of Tp_2Mn in toluene-d_8. Bottom: at 298 K; the calculated signal shifts are shown as red bars, from left: H4, H5, H3, BH. S = residual solvent protons, * = impurities. The spectrum deconvolution shows three signals (blue) and their sum (yellow). Top: at 379 K (see text).

No analyzable features could be detected in the ^{13}C NMR spectrum of Tp_2Mn and the ^{11}B NMR signal was found to be 10% less negative than reported previously (–112 ppm).[23]

The theoretical ^{1}H NMR shifts of Tp_2Mn and Tp^*_2Mn are generally in good agreement with experiment, with the exception of H4 in Tp^*_2Mn, where theory overestimates the measured signal shift by 18 ppm.

Table 8. Signal Shifts of Tp_2Mn and Tp^*_2Mn.

Nuclear position	3	Me3	4	5	Me5	BH
			Tp_2Mn			
δ^{exptl} (^{1}H)[a]	4.6		50.6	31.1		−3.5
δ^{calcd} (^{1}H)[a]	14.5		58.3	27.9		−4.0
δ^{calcd} (^{13}C)[a]	1310.7		485.3	896.8		
other shifts	δ^{exptl} (^{11}B)[a] = −101; δ^{calcd} (^{11}B)[a] = −117.4 δ^{exptl} (^{14}N1) [b] ; δ^{calcd} (^{14}N1)[a] = 1170.1					
			Tp^*_2Mn			
δ^{exptl} (^{1}H)[c]		18	31		20	−2
δ^{calcd} (^{1}H)[c]		21.3	48.9		24.5	−1.1
δ^{calcd} (^{13}C)[a]	1325.2	11.5	493.1	861.1	34.5	
other shifts	δ^{exptl} (^{11}B) [b] ; δ^{calcd} (^{11}B)[a] = −105.9 δ^{exptl} (^{14}N1) [b] ; δ^{calcd} (^{14}N1)[a] = 1142.9					

[a] 298 K. [b] Signal could not be localized in an extended range. [c] 379 K.

As expected from the NMR signal widths, Tp_2Mn may also be studied using EPR spectroscopy. Thus, for a 1% solid solution in Tp_2Zn at 128 K, the features of five spin transitions in *x*, *y*, and *z* directions can be observed. They yield D = 0.052 cm^{-1}, E = 0.0098 cm^{-1}, and A(^{55}Mn) = 258 MHz.[57] The computations of the ZFS and *g*-tensors (Table SI23) agree with a very small spin-orbit -coupling in these systems, leading to minute ZFS and only modest deviation of the *g*-tensor from the isotropic free-electron value.

Corresponding to the minor role played by the spin-orbit coupling, the paramagnetic parts of the shieldings of Tp_2Mn and Tp^*_2Mn are very strongly determined by the contact term 1, with only very small contributions by the “dip” and “con,3” terms 2 and 6 (Tables SI28-SI30).

d^4, Tp_2Cr, Tp^*_2Cr, S = 2. Owing to rather narrow and well-separated signals, the proton NMR spectra of Tp_2Cr and Tp^*_2Cr (Figures SI17 and SI18) can be analyzed straightforwardly. This is even more striking for the ^{13}C NMR spectra (Figures 10 and SI19) where signals shifted more than 1100 ppm are observed without resorting to high temperatures. The signal assignment relies on the signal-width criterion, the

signal areas (Tp^*_2Cr), and the comparison of the respective spectra of Tp_2Cr and Tp^*_2Cr. The signal shifts and half widths are collected in Tables 9 and SI34, respectively. An overall satisfactory agreement with ^1H and ^{13}C measurements is obtained in the quantum-chemical calculations.

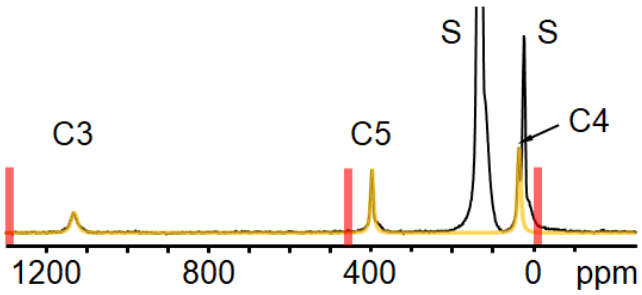

Figure 10. ^{13}C NMR spectrum of Tp_2Cr in toluene at 305 K. The calculated signal shifts are shown as red bars, from left: C3, C5, C4. S = solvent signal. Yellow trace: simulated spectrum.

Table 9. Signal Shifts of Tp_2Cr and Tp^*_2Cr.

Nuclear position	3	Me3	4	5	Me5	BH
			Tp_2Cr			
δ^{exptl} (^{1}H)[a]	−36.7		21.5	−9.9		6.4
δ^{calcd} (^{1}H)[a]	−45.8		29.7	−23.4		8.4
δ^{exptl} (^{13}C)[a]	1131		35.0	396		
δ^{calcd} (^{13}C)[a]	1287.9		−9.6	455.3		
other shifts	δ^{exptl} (^{11}B)[b] = −80.9; δ^{calcd} (^{11}B)[b] = −112.5 δ^{exptl} (^{14}N1) = [c] ; δ^{calcd} (^{14}N1)[b] = 1055.6					
			Tp^*_2Cr			
δ^{exptl} (^{1}H)[a]		41.7	21.7		39.9	8.2
δ^{calcd} (^{1}H)[a]		56.2	28.2		50.3	9.8
δ^{exptl} (^{13}C)[b]	1104	−25.8	16.5	422	−40.5	
δ^{calcd} (^{13}C)[b]	1255.1	−41.5	−42.0	476.3	−51.6	
other shifts	δ^{exptl} (^{11}B) = [c] ; δ^{calcd} (^{11}B)[b] = −87.6 δ^{exptl} (^{14}N1) = [c] ; δ^{calcd} (^{14}N1)[b] = 1070.7					

[a] 305 K. [b] 298 K. [c] Not observed.

These systems are characterized by ZFS *D*-parameter around -2 cm^{-1} and a comparatively small, albeit larger than in the d^5 Mn systems above, deviation of the *g*-tensor from the isotropic free-electron value (Table SI23). Similarly to the Mn complexes, the paramagnetic shieldings of Tp_2Cr and Tp^*_2Cr are strongly dominated by the contact term 1. A significant contribution to C3 is obtained from the "con,3" term 6 (Tables SI28- SI30).

d^3, $[Tp_2Cr]^+[PF_6]^-$, Tp_2V, and Tp^*_2V, S = 3/2. Ions with d^3 and S = 3/2 configuration such as Cr^{3+} and V^{2+} are further cases where slow electron relaxation rates lead to broad NMR signals.[54,55] Actually, even at high temperature, the proton NMR spectrum of $[Tp_2Cr][PF_6]$ shows only three instead of the expected four signals (Figure SI20). They are broad and partly overlapping; no further signal could be found in the range ±150 ppm. The signal assignment follows the calculated shifts, and Table 10 shows good agreement between theoretical and experimental data. We

cannot exclude that the signal of H5 coincides with the missing signal of H3. Then the assignment on passing to decreasing signal shifts should be BH, H4, H5/H3.

For Tp_2V, two proton signals could be identified (Figure SI21) and for Tp^*_2V only one. Again, the theoretical shifts are the only assignment criterion, and even then the signal of Tp^*_2V may belong to either H4 or BH. Here we opt for H4 because, generally, the signals of H4 are much narrower than those of BH (Table SI33) and thus, in the case of Tp^*_2V, the BH signal (besides those of H5 and H3) disappeared in the baseline.

For the ^{13}C NMR spectra of $[Tp_2Cr]^+[PF_6]^-$ and Tp_2V limitations similar to the proton spectra were met. Thus, only one signal could be detected in each case. It should be that of C5 as suggested by the theoretical shifts (Table 10). The measured ^{11}B NMR signal shift of $[Tp_2Cr]^+[PF_6]^-$ is in good accord with the theoretical result for $[Tp_2Cr]^+$.

Powder EPR spectra of $[Tp_2Cr][PF_6]$ at various temperatures show patterns for three transitions along each of the three directions in space with g_{zz} = 1.9646 for the central transition. Other data are D = 0.187 cm^{-1} and E = 0.01 cm^{-1}.[58] The present calculations (Table SI23) are in good correspondence with these data. As expected, similar spectra were obtained for Tp^*_2V (10^{-3} molar solid solution in toluene at 4 K): g_{zz} = 2.0809, D = 0.234 cm^{-1}, E ~ 0 cm^{-1}.[58]

Table 10. Signal Shifts of $[Tp_2Cr]^+[PF_6]^-$, Tp_2V and Tp^*_2V.

Nuclear position	3	Me3	4	5	Me5	BH
			$[Tp_2Cr]^+$			
δ^{exptl} (^{1}H)[a]	–45		–11.4	–45		10.9
δ^{calcd} (^{1}H)[a]	–43.8		–0.9	–35.3		8.2
δ^{exptl} (^{13}C)[b]	[c]		[c]	180		
δ^{calcd} (^{13}C)[b]	640.7		–288.1	172.3		
other shifts	δ^{exptl} (^{11}B)[b] = –40.3; δ^{calcd} (^{11}B)[b] = –56.5 δ^{exptl} (^{14}N1) = [c] ; δ^{calcd} (^{14}N1)[b] = 244.2					
			Tp_2V			
δ^{exptl} (^{1}H)[d]	[c]		[c]	–25		4.8
δ^{calcd} (^{1}H)[d]	–85.0		19.2	–45.0		11.3
δ^{exptl} (^{13}C)[e]	[f]	[f]	[f]	284	[f]	
δ^{calcd} (^{13}C)[e]	1244.7		-250.6	316.9		
other shifts	δ^{exptl} (^{11}B) = [f] ; δ^{calcd} (^{11}B)[b] = –155.7 δ^{exptl} (^{14}N1) = [c] ; δ^{calcd} (^{14}N1)[b] = 1573.7					
			Tp^*_2V			
δ^{exptl} (^{1}H)[g]		[c]	9.4		[c]	[c]
δ^{calcd} (^{1}H)[g]		79.6	16.8		65.2	14.6
δ^{calcd} (^{13}C)[b]	1419.2	–121.5	–391.7	418.1	–125.7	
other shifts	δ^{exptl} (^{11}B) = [f] ; δ^{calcd} (^{11}B)[b] = –114.9 δ^{exptl} (^{14}N1) = [f] ; δ^{calcd} (^{14}N1)[b] = 1606.5					

[a] 455 K. [b] 298 K. [c] Not observed. [d] 379 K. [e] 380 K. [f] Not measured. [g] 349 K.

The computations of ZFS parameters and *g*-tensors indicate, for all the three systems, a small ZFS *D*-parameter and an isotropic *g*-tensor below the free-electron *g*-value (Table SI23). All of the paramagnetic shieldings of Tp_2V, Tp^*_2V and $[Tp_2Cr]^+$ are dominated by the contact term 1 (with minor modification from the “con,3” term 6

for carbon, boron and nitrogen), as was the case with the Mn and Cr complexes (Tables SI28-SI30).

d^2, $[Tp_2V]^+[B(C_6H_5)_4]^-$ and $[Tp^*_2V]^+[B(C_6H_5)_4]^-$, *S* = 1. Both compounds yield ^1H NMR spectra showing narrow signals except for those of H3 (Figures SI22 and SI23). The theory suggests that the BH signal of $[Tp^*_2V]^+$ interferes with the signals H2'-H6' of $[B(C_6H_5)_4]^-$ but this could not be assured. The assignment of the signals based on their widths and shifts (Table 11) differ partly from the shift calculations, which is not unusual given the rather small shift range.

Table 11. Signal Shifts of $[Tp_2V]^+[B(C_6H_5)_4]^-$ and $[Tp^*_2V]^+[B(C_6H_5)_4]^-$.

Nuclear position	3	Me3	4	5	Me5	BH
			$[Tp_2V]^+$			
δ^{exptl} (^1H)[a]	−21.7		8.8	5.8		[c]
δ^{calcd} (^1H)[a]	−14.9		11.4	−5.2		−2.4
δ^{exptl} (^{13}C)[a]	540.3		−22.7[b]	156.9[c]		
δ^{calcd} (^{13}C)[a]	553.4		−35.8	161.6		
other shifts	δ^{exptl} (^{11}B)[d] = −13.1; δ^{calcd} (^{11}B)[d] = −69.6 δ^{exptl} ($^{14}N1$) = [e] ; δ^{calcd} ($^{14}N1$)[d] = 555.6					
			$[Tp^*_2V]^+$			
δ^{exptl} (^1H)[a]		18.9	5.6		18.4	[e]
δ^{calcd} (^1H)[a]		27.0	7.4		19.3	1.5
δ^{exptl} (^{13}C)[d]	510	−45.0	−50[f]	201	0.0	
δ^{calcd} (^{13}C)[d]	523.2	−39.2	−63.5	204.1	−6.0	
other shifts	δ^{exptl} (^{11}B)[d] = −12.2; δ^{calcd} (^{11}B)[d] = −60.5 δ^{exptl} ($^{14}N1$) = [g] ; δ^{calcd} ($^{14}N1$)[d] = 777.3					

[a] 305 K. [b] ^1J(C,H) = 180 ± 3 Hz. [c] ^1J(C,H) = 186 ± 3 Hz. [d] 298 K. [e] Not observed. [f] Signal partly hidden under the signal of Me3. [g] Not measured.

By contrast, for $[Tp_2V]^+$ the agreement of the theoretical and experimental ^{13}C NMR result is excellent (Figure 11 and Table 11). Owing to favorable relaxation the coupling constants, ^1J(C,H) of C4 and C5 can be observed.

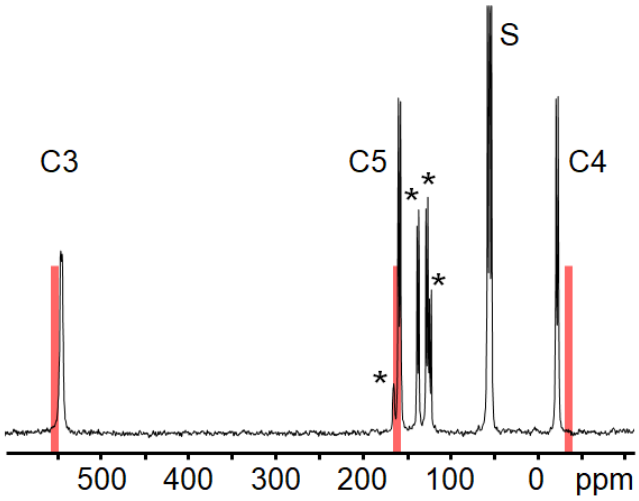

Figure 11. ^{13}C NMR spectrum of $[Tp_2V]^+[B(C_6H_5)_4]^-$ in CH_2Cl_2 at 305 K. * = signals of the anion, from left: C1′, C2′/6′, C3′/5′, C4′. The calculated signal shifts of $[Tp_2V]^+$ are shown as red bars, from left: C3, C5, C4. S = solvent.

The ^{13}C NMR signals of $[Tp^*_2V]^+$ are considerably broader (Figure SI24 and Table SI34), notably those of C3 and C4. The calculated signal shifts were essential for identifying these signals. For the remaining signals of C5, Me3, and Me5 the calculated and experimental shifts are again in a very good agreement (Figure SI24 and Table 11). On the other hand, the calculated ^{11}B signal shifts fail to reproduce experimental results in $[Tp_2V]^+$ and $[Tp^*_2V]^+$, with a significant disagreement in both cases. Spin-orbit coupling in these systems is large, as indicated by the sizable ZFS *D*-parameter at -40 and -27 cm^{-1} for $[Tp_2V]^+$ and $[Tp^*_2V]^+$, respectively, as well as large and anisotropic *g*-shifts (Table SI23).

The source of paramagnetic shielding of $[Tp_2V]^+$ and $[Tp^*_2V]^+$ varies with nuclear position, with practically all the terms giving important contributions, as befitting the large spin-orbit coupling in these systems. The contact and pseudocontact terms 1 and 9 are usually the most significant contributors (Tables SI28-SI30).

NMR FEATURES of the $Tp^{(*)}{}_2M$ SERIES AND CONCLUSIONS

Experimental aspects. The NMR spectra of paramagnetic Tp_2M derivatives provide valuable information when the signals are narrow enough to be recorded with routine spectrometer setup, in particular when the signal assignment can be assured. This confirms the power of pNMR, to which recent studies of paramagnetic transition metal complexes and organometallic compounds in solution have contributed major advances.[73,74,75,76,77,78,7980]

The series Tp_2M and $Tp^*{}_2M$ indicate that NMR studies of Tp_2M derivatives are most rewarding when M is Ni(II), Co(II), Fe(II), Fe(III), Cr(II), or V(III). The spectra of compounds with M = Cu(II), Mn(II), Cr(III), and V(II) have distinctly broader signals but are useful to complement the corresponding EPR spectra. Thus, the NMR spectra yield information on the periphery of these compounds represented by the nuclei ^1H, ^{11}B, ^{13}C, and ^{14}N, while EPR spectra would show light on the metal centers and the first coordination sphere. The overall magnetic resonance behavior reflects the different electron relaxation of such species.[25,54,55]

A closer inspection reveals that, besides ^1H, ^{13}C is an important nucleus to study. ^{13}C NMR spectra are expected to provide even richer information than proton spectra for ligands such as $[Tp^{Br}{}_3]^-$.[81] Owing to the larger signal shift spread, ^{13}C NMR spectra are usually better resolved, even though a given ^{13}C signal is often broader than the corresponding proton signal. The latter finding is mainly due to the fact that the signal widths depend on the distance between the respective nucleus and the metal center (see Supporting Information). In favorable cases, comparable ^1H and ^{13}C widths are found; examples are Tp_2Co and $[Tp_2Fe]^+$. The couplings ^1J(C4,H) and ^1J(C5,H) of Tp_2Co, Tp_2Fe, $[Tp_2Fe]^+$, and $[Tp_2V]^+$ correspond to those of diamagnetic TpK[82] within the error limits. Thus, a partial alignment of the molecules in the external magnetic field, as observed for Tp_2Co derivatives,[83,84] and the known effect on ^1J(C,H)[85] is not visible under our experimental conditions. ^{11}B and ^{14}N attract interest when local magnetic moments and spin densities are concerned. When passing from Tp_2M to $Tp^*{}_2M$ the signal widths increase throughout the series (Table SI34). This is most noticeable when, due to less favorable electron spin relaxation, the signals are somewhat broader anyway. It can be ascribed to the molecular tumbling time contributing to the overall relaxation time and the fact that small molecules tumble faster.

The signal assignment is significantly and efficiently supported by the theoretical calculations of the signal shifts. Not only does the theory confirm assignments based on different signal intensities and on the signal widths, often theory is the only means to assign a signal and thus to explore properties such as the molecular structure,

dynamic behavior, spin crossover, magnetic interaction, and spin delocalization as documented for other cases.[25,54,86,87,88,89,90]

Computational accuracy. Although qualitative match between theory and experiment is obtained and aids in the assignment of signals, the computations reproduce experimental spectra quantitatively only on occasion. There are several factors that may contribute to this. Deficiencies in basis sets and the choice of the DFT functional can impact, in particular, the hyperfine coupling tensors. Zero-field splitting and the *g*-tensor, which are presently calculated using *ab initio* methods, are currently less sensitive to computational choices within that realm. Solvation effects were generally neglected presently, including the interactions between the charged molecules and their counterions. The effects of explicit solvent molecules were studied for $[Tp_2Fe]^+$. Intramolecular dynamics were likewise ignored. The restriction of the used pNMR formalism to the ground-state multiplet, parameterized by EPR parameters, may cause severe errors with molecules containing low-lying excited states, as was hinted at by the study done with $[Tp_2Fe]^+$. For this system it is notable that reassignment of the experimental ^{13}C shifts would re-establish qualitative agreement of the present calculations with experiment, at least when the variation of the computational results with the DFT functional employed in HFC calculations is taken into account. Such a reassignment would not be in line with the experimental linewidth information, however.

In the case of the spin-crossover system Tp_2Fe, consideration of both the diamagnetic singlet (S = 0) state and the paramagnetic quintet (S = 2) state was required to explain the experimental temperature dependence of ^1H chemical shifts. A Boltzmann-weighted mixture of the states with the inclusion of entropy achieved qualitative agreement with the experimental temperature dependence of ^1H shifts.

The impact of electron correlation on the accuracy of computed EPR parameters bears further discussion. In previous studies[26,28,34] involving the calculation of the ZFS and the *g*-tensor at the CASSCF/NEVPT2 level, correlating the metal 3d-orbitals has been found to work reasonably well for the purpose of estimating pNMR shieldings. However, this choice of active orbitals is a compromise and leads to, for instance, overestimation of the *D*-parameter. The impact of inaccuracies in *ab initio* calculations of ***g*** and ZFS on the calculated pNMR shifts is minor, however, in comparison with the quality of the HFC data by DFT.[91]

Another important point to consider is the sensitivity of hyperfine couplings to the choice of DFT functional. As seen previously,[51,92,93,] the amount of exact exchange admixture in hybrid functionals is a significant factor affecting the accuracy of results. A common choice is the PBE0 functional with 25 percent exact exchange, primarily used in this study. Although it is often possible to gain good compatibility with experiment for a certain nucleus in a certain molecule by empirically optimizing the portion of exact exchange, it has so far proven impossible to find a good “universal” value for the exact exchange parameter that would systematically improve results across the board.

The series of transition-metal pyrazolylborate systems represents a wide range of different physical situations arising from the electronic structure of the metal centers. The present computations allow a detailed investigation of the microscopic mechanisms behind the observed pNMR chemical shifts. A general finding is that the systems with significant spin-orbit coupling effects, evidenced by the large deviation of the *g*-tensor from the free-electron *g*-factor, a large anisotropy of the *g*-tensor, as well as a significant value of the *D*-parameter of ZFS, are characterized by large shift contributions other than the contact shift. Such contributions include the pseudocontact shift (term 9, Table SI1), involving the dipolar HFC and the anisotropy of ***g***, as well as the leading-order dipolar shift (term 2), which only contributes to the isotropic shielding due to the ZFS interaction.[94]

A summary comparison of 128 pairs of experimental and theoretical signal shifts is shown in Figure 12. According to linear regression ($\delta^{\mathrm{calcd}} = 1.061\ \delta^{\mathrm{exptl}}$, R = 0.9947) the best-fit line passes through the origin and its slope is virtually one. There is some data point scatter, notably in the regions 200 to 300 ppm and 550 to 700 ppm, but the overall result encourages further work.

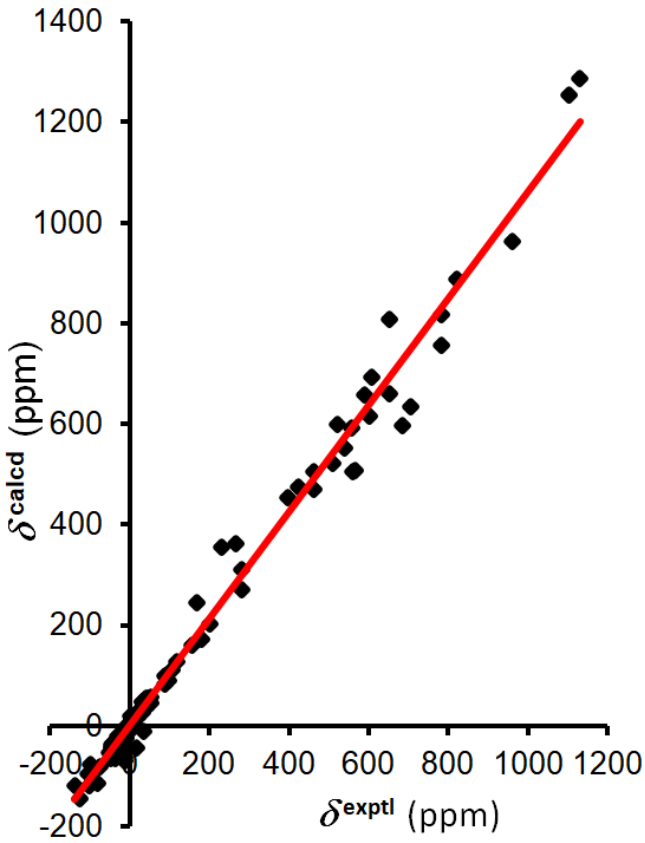

Figure 12. Plot of the calculated versus experimental ^{1}H, ^{11}B, ^{13}C, and ^{14}N NMR signal shifts of the series Tp_2M, Tp^*_2M, $[Tp_2M]^+$, and $[Tp^*_2M]^+$ except for the ^{13}C data of $[Tp^{(*)}_2Fe]^+$ discussed above.

ASSOCIATED CONTENT

Supporting Information

The Supporting Information is available free of charge at.....

Theoretical calculations: Physical contributions to the nuclear shielding, Optimized geometries, *D*- and *E*-parameters of ZFS and *g*-tensors, Additional tables for computed shieldings. Experimental procedures: Syntheses, NMR spectroscopy. pNMR signal widths and interatomic distances. Additional ^{1}H and ^{13}C NMR spectra. Spin crossover in Tp_2Fe: Thermodynamic data from classical analysis of the ^{1}H NMR shifts.

AUTHOR INFORMATION

Corresponding Authors

Juha Vaara - *NMR Research Unit, University of Oulu, P.O. Box 3000, Oulu FI-90014, Finland;* orcid.org/0000-0002-1179-4905; Email: juha.vaara@ oulu.fi

Frank H. Köhler - *Department Chemie, Technische Universität München, D-85748 Garching, Germany;* orcid.org/0000-0002-4324-0018; Email: f.h.koehler@lrz.tum.de

Authors

Ari Pyykkönen - *NMR Research Unit, University of Oulu, P.O. Box 3000, Oulu FI-90014, Finland;* Email: ari.pyykkonen@oulu.fi

Robert Feher - *Department Chemie, Technische Universität München, D-85748 Garching, Germany;* present address: *Graphit Kropfmühl GmbH, Langheinrichstraße 1, 94051 Hauzenberg, Germany;* Email: stepll@hotmail.com

Notes

The authors declare no competing financial interest.

ACKNOWLEDGEMENTS

This work was funded by the Academy of Finland (grant 296292) and University of Oulu (Kvantum Institute). Computational resources were provided by CSC-IT Center for Science (Espoo, Finland) and the Finnish Grid and Cloud Infrastructure project (persistent identifier urn:nbn:fi:research-infras-2016072533).

(1)Trofimenko, S. Boron-Pyrazole Chemistry *J. Am. Chem. Soc.* **1966**, *88*, 1842-1844.
(2) Trofimenko, S. The Coordination Chemistry of Pyrazole-Derived Ligands *Progr. Inorg. Chem.* **1986**, *34*, 115-210.
(3) Trofimenko, S. *Scorpionates: The Coordination Chemistry of Poly(pyrazolyl)borate Ligands*; Imperial College Press: London, 1999.
(4) Pettinari, C.; Trofimenko, S. *Scorpionates II: Chelating Borate Ligands;* Imperial College Press: London, 2008.
(5) Limberg, C.; Sallmann, M. Utilizing the Trispyrazoly Borate Ligand for Mimiking of O_2-Activating Mononuclear Nonheme Enzymes *Acc. Chem. Res.* **2015**, *48*, 2734-2743.
(6) Pellei, M.; Santini, C. (April 26th 2011) Biomimetic Applications of Metal Systems Supported by Scorpionates, Biomimetic Based Applications, Anne George, IntechOpen, DOI: 10.5772/14854. Available from: https://www.intechopen.com/books/biomimetic-based-applications/biomimetic-applications-of-metal-systems-supported-by-scorpionates.
(7) Cummins, D. C.; Yap, D. P. A.; Theopold, K. H. Scorpionates of the "Tetrahedral Enforcer" Variety as Ancillary Ligands for Dinitrogen Complexes of First Row Transition Metals (Cr-Co) *Eur. J. Inorg. Chem.* **2016**, 2349-2356.
(8) Hikichi, S.; Akita, M.; Moro-oka, Y. New Aspects of the Cobalt-Diogygen Complex Chemistry Opened by Hydrotris(pyrazoly)borate Ligands (TP^R): Unique Properties of Tp^RCo-Diogygen Complexes *Coord. Chem. Rev.* **2000**, *198*, 61-87.
(9) Long, G. J.; Grandjean, F.; Reger, D. L. Spin Crossover in Pyrazolyborate and Pyrazolymethane Complexes *Topics Curr. Chem.* **2004**, *233*, 91-122.
(10) Zang, Y.; Malik, U. P.; Quiggins, B.; Nguyen, H.; Beedle, C. C.; Kovalev, A. E.; Clérac, R.; Hill, S.; Bythell, B. J.; Holmes, S. M. Structure-Property Relationships in Tricyanoferrate (III) Building Blocks and Trinuclear Cyanide-Bridged Complexes *Eur. J. Inorg. Chem.* **2016**, 2432-2442.
(11) Wang, S.; Ding, X.-H.; Zuo, J.-L.; You, X.-Z.; Huang, W. Tricyanometalate Molecular Chemistry: A Type of Versatile Building Blocks for the Construction of Cyano-Bridged Molecular Architectures *Coord. Chem. Rev.* **2011**, *255*, 1713-1732.
(12) Lescouëzec, R.; Toma, L. M.; Vaissermann, J.; Verdaguer, M.; Delgado, F. S.; Ruiz-Pérez, C.; Lloret, F.; Julve, M. Design of Single Chain Magnets through Cyanide-Bearing Six-Coordinate Complexes *Coord. Chem. Rev.* **2005**, *249*, 2691-2729.
(13) McKeown, B. A.; Lee, J. P.; Mei, J.; Cundari, T. R.; Gunnoe, T. B. Transition Metal Mediated C-H Activation and Functionalization: The Role of Poly(pyrazolyl)borate and Poly(pyrazolyl)alkane Ligands *Eur. J. Inorg. Chem.* **2016**, 2296-2311.
(14) Wathier, M.; Love, J. A. Hydroelementation of Unsaturated C-C Bonds Catalyzed by Metal Scorpionate Complexes *Eur. J. Inorg. Chem.* **2016**, 2391-2402.
(15) Reinig, R. R.; Mukherjee, D.; Weinstein, Z. B.; Xie, W.; Albright, T.; Baird, B.; Gray, T. S.; Ellern, A.; Miller, G. J.; Winter, A. H.; Bud'ko, S. L.; Sadow, A. D. Synthesis and Oxidation Catalysis of [Tris(oxazolinyl)borato]cobalt(II) Scorpionates *Eur. J. Inorg. Chem.* **2016**, 2486-2494.
(16) Chakraborty, S.; Piszel, P. E.; Brennessel, W.; Jones, W. D. A Single Nickel Catalyst for the Acceptorless Dehydrogenation of Alcohols and Hydrogenation of Carbonyl Compounds *Organometallics* **2015**, *34*, 5203-5206.

(17) Camasso, N. M.; Sanford, M. S. Design, Synthesis, and Carbon-Hetroatom Coupling Reactions of Organometallic Nickel (IV) Complexes *Science* **2015**, *347*, 1218-1220.
(18) Pawar, G. M.; Shaeridan, J. B.; Jäkle, F. Pyridylborates as a New Type of Robust Scorpionate Ligand: From Metal Complexes to Polymeric Materials *Eur. J. Inorg. Chem.* **2016**, 2227-2235.
(19) Camerano, J. A.; Casado, M. A.; Ciriano, M. A.; Oro, L. A. Tris(pyrazoly)borate Dendrimers and Metallodendrimers *Dalton Trans.* **2006**, 5287-5293.
(20) Kammerer, C.; Rapenne, G. Scorpionate Hydrotris(indazolyl)borate Ligands as Tripodal Platforms for Surface-Mounted Molecular Gears and Motors *Eur. J. Inorg. Chem.* **2016**, 2214-2226.
(21) Zao, T.; Boldog, I.; Spasojevic, V.; Rotaru, A.; Garcia, Y.; Janiak, C. Solvent-Triggered Relaxative Spin State Switching of $[Fe(HB(pz)_3)_2]$ in a Closed Nano-Confinement of NH_2-MIL-101(Al) *J. Mater. Chem. C* **2016**, *4*, 6588-6601.
(22) Jesson, J. P.; Trofimenko, S.; Eaton, D. R. Spectra and Structure of Some Transition Metal Poly(1-pyrazolyl)borates *J. Am Chem. Soc.* **1967**, *89*, 3148-3158.
(23) Jesson, J. P. Isotropic Nuclear Resonance Shifts in Some Trigonal Co(II) and Ni(II) Chelate Systems *J. Chem. Phys.* **1967**, *47*, 582-591. Data from ref. 23 cited here follow the new shift sign convention, they were converted to 298 K by assuming that the measuring temperature was 303 K as in ref. 22, and the ^{11}B data were calculated relative to the now common reference $BF_3(Et_2O)$.
(24) Jesson, J. P.; Trofimenko, S.; Eaton, D. R. Spin Equilibria in Octahetral Iron(II) Poly(1-pyrazolyl)borates *J. Am Chem. Soc.* **1967**, *89*, 3158-3164.
(25) *NMR of Paramagnetic Molecules*; La Mar, G. N.; Horrocks, Jr., W. D.; Holm, R. H., Eds.; Academic Press: New York, 1973.
(26) Rouf, S. A.; Mareš, J.; Vaara, J. ^1H Chemical Shifts in Paramagnetic Co(II) Pyrazolylborate Complexes: A First-Priciples Study *J. Chem. Theory Comput.* **2015**, *11*, 1683-1691.
(27) Van den Heuvel, W.; Soncini, A. NMR Chemical Shift as Analytical Derivative of the Helmholtz Free Energy *J. Chem. Phys.* **2013**, *138*, 054113.
(28) Vaara, J.; Rouf, S. A.; Mareš, J. Magnetic Couplings in the Chemical Shift of Paramagnetic NMR *J. Chem. Theory Comput.* **2015**, *11*, 4840-4849.
(29) Kurland, R.J.; McGarvey, B. R. Isotropic NMR Shifts in Transition Metal Complexes: The Calculation of the Fermi Contact and Pseudocontact Terms *J. Mag. Res.* **1970**, *2*, 286-301.
(30) Gendron, F.; Sharkas, K.; Autschbach, J. Calculating NMR Chemical Shifts for Paramagnetic Metal Complexes from First-Principle *J. Phys. Chem. Lett.* **2015**, *6*, 2183-2188.
(31) Moon, S.; Patchkovskii, S. in *Calculation of NMR and EPR Parameters*, eds. Kaupp, M.; Bühl, M.; Malkin, V. G. Wiley-VCH Verlag GmbH & Co. KGaA, Weinheim, FRG, **2004**, pp. 325–338.
(32) Pennanen, T. O.; Vaara, J. Density-Functional Calculations of Relativistic Spin-Orbit Effects on Nuclear Magnetic Shielding in Paramagnetic Molecules *J. Chem. Phys.* **2005**, *123*, 174102.
(33) Arbuznikov, A. V.; Vaara, J.; Kaupp, M. Relativistic Spin-Orbit Effects on Hyperfine Coupling Tensors by Density-Functional Theory *J. Chem. Phys.* **2004**, *120*, 2127-2139.
(34) Rouf, S. A.; Mareš, J.; Vaara, J. Relativistic Approximations tp Paramagnetic NMR Chemical Shift and Shielding Anisotropy in Transition Metal Systems *J. Chem. Theory Comput.* **2017**, *13*, 3731-3745.

(35) TURBOMOLE V7.2 2017, a development of University of Karlsruhe and Forschungszentrum Karlsruhe GmbH, 1989-2007, TURBOMOLE GmbH, since 2007; available from http://www.turbomole.com.
(36) Adamo, C.; Barone, V.Toward Reliable Density Functional Methods without Adjustable Parameters:The PBEO Model *J. Chem. Phys.* **1999**, *110*, 6158−6170.
(37) Grimme, S.; Antony, J.; Ehrlich, S.; Krieg, H. A Consistent and Accurate *ab initio* Parametrization of Density Functional Dispersion Correction (DFT-D) for the 94 Elements H-Pu *J. Chem. Phys.* **2010**, *132*, 154104.
(38) Grimme, S.; Ehrlich, S.; Goerigk, L. Effect of the Damping Function in Dispersion Corrected Density Functional Theory *J. Comput. Chem.* **2011**, *32*, 1456-1465.
(39) Weigend, F.; Ahlrichs, R. Balanced Basis Sets of Split Valence, Triple Zeta Valence and Quadrupole Zeta Valence Quality for H to Rn: Design and Assessment of Accuracy *Phys. Chem. Chem. Phys.* **2005**, *7*, 3297−3305.
(40) Dolg, M.; Wedig, U.; Stoll, H.; Preuß, H. Enery-Adjusted ab initio Pseudopotentials for the First Row Transition Elements *J. Chem. Phys.* **1987**, *86*, 866−872.
(41) Angeli, C.; Cimiraglia, R.; Evangelisti, S.; Leininger, T; Malrieu, J.-P. Introduction of n-Electron Valence States for Multireference Perturbation Theory *J. Chem. Phys.* **2001**, *114*, 10252-10264.
(42) Angeli, C.; Cimiraglia, R.; Malrieu, J.-P. n-Electron Valence State Perturbation Theory: A Fast Implementation of the Strongly Contracted Variant *Chem. Phys. Lett.* **2001**, *350*, 297-305.
(43) Angeli, C.; Cimiraglia, R.; Malrieu, J.-P. n-Electron Valence State Perturbation Theory: A Spinless Formulation and an Efficient Implementation of the Strongly Contracted and of the Partially Contracted Variants *J. Chem. Phys.* **2002**, *117*, 9138-9153.
(44) Roos, B. O. A New Method for Large-Scale CI Calculations *Chem. Phys. Lett.* **1972**, *15*, 153−159.
(45) Pantazis, D. A.; Chen, X. Y.; Landis, C. R.; Neese, F. All-Electron Scalar Relativistic Basis Sets for Third-Row Transition Metal Atoms *J. Chem. Theory Comput.* **2008**, *4*, 908-919.
(46) Douglas, M.; Kroll, N. M. Quantum Electrodynamical Corrections to the Fine Structure of Helium *Ann. Phys.* **1974**, *82*, 89−155; **1989**, *191*, 399; Hess, B. A. Relativistic Electron-Structure Calculations Employing a Two-Component No-Pair Formalism with External-Field Projection Operators *Phys. Rev. A: At., Mol., Opt. Phys.* **1986**, *33*, 3742−3748.
(47) Ganyushin, D.; Neese, F. First-Principle Calculations of Zero-Field Splitting Parameters *J. Chem. Phys.* **2006**, *125*, 024103; **2013**, *138*, 104113.
(48) Neese, F. The ORCA Program System *Wiley Interdiscip. Rev.: Comput. Mol. Sci.* **2012**, *2*, 73-78.
(49) Malkin E.; Repisky M.; Komorovsky S.; Mach P.; Malkina O. L.; Malkin V. G. Effects of Finite Size Nuclei in Relativistic Four-Component Calculations of Hyperfine Structure *J. Chem. Phys.* **2011**, *134*, 044111.
(50) Dyall, K. G.; Gomes A. S. P.; unpublished, see documentation of the Dirac software in http://dirac.chem.sdu.dk/basisarchives/dyall/.
(51)Gohr, S.; Hrobárik, P.; Repisky, M.; Komorovsky, S.; Ruud, K.; Kaupp, M. Four-Component Relativistic Density Functional Theory Calculations of EPR g- and Hyperfine-Coupling Tensors Using Hybrid Functionals: Validation on Transition-Metal Complexes with Large Tensor Anisotropies and Higher-Order Spin–Orbit Effects *J. Phys. Chem. A* **2015**, *119*, 12892-12905.

(52) **ReSpect**, version 3.4.2 (2015); Relativistic Spectroscopy DFT program of authors Repisky, M.; Komorovsky, S.; Malkin, V. G.; Malkina, O. L.; Kaupp, M.; Ruud, K., with contributions from Bast, R.; Ekstrom, U.; Kadek, M.; Knecht, S.; Konecny, L.; Malkin, E.; Malkin-Ondik, I. (see www.respectprogram.org).
(53) Gaussian 09, Revision E.01, M. J. Frisch, G. W. Trucks, H. B. Schlegel, G. E. Scuseria, M. A. Robb, J. R. Cheeseman, G. Scalmani, V. Barone, G. A. Petersson, H. Nakatsuji, X. Li, M. Caricato, A. Marenich, J. Bloino, B. G. Janesko, R. Gomperts, B. Mennucci, H. P. Hratchian, J. V. Ortiz, A. F. Izmaylov, J. L. Sonnenberg, D. Williams-Young, F. Ding, F. Lipparini, F. Egidi, J. Goings, B. Peng, A. Petrone, T. Henderson, D. Ranasinghe, V. G. Zakrzewski, J. Gao, N. Rega, G. Zheng, W. Liang, M. Hada, M. Ehara, K. Toyota, R. Fukuda, J. Hasegawa, M. Ishida, T. Nakajima, Y. Honda, O. Kitao, H. Nakai, T. Vreven, K. Throssell, J. A. Montgomery, Jr., J. E. Peralta, F. Ogliaro, M. Bearpark, J. J. Heyd, E. Brothers, K. N. Kudin, V. N. Staroverov, T. Keith, R. Kobayashi, J. Normand, K. Raghavachari, A. Rendell, J. C. Burant, S. S. Iyengar, J. Tomasi, M. Cossi, J. M. Millam, M. Klene, C. Adamo, R. Cammi, J. W. Ochterski, R. L. Martin, K. Morokuma, O. Farkas, J. B. Foresman, and D. J. Fox, Gaussian, Inc., Wallingford CT, 2016.
(54) Bertini, I.; Luchinat, C.; Parigi, G. Ravera, E. *NMR of Paramagnetic Molecules*; Elsevier: Amsterdam, The Netherlands, 2016; Chapter 4.
(55) Pell, A. J.; Pintacuda, G.; Grey, C. P. Paramagnetic NMR in Solution and the Solid State *Prog. Nucl. Magn. Reson. Res. Spectrosc.* **2019**, *111*, 1-271.
(56) Murphy, A.; Hathaway, B. J.; King, T. J. Single-Crystal Structure and Electronic Properties of Bis[hydrotris(pyrazolyl-1)borato]copper(II) *J. Chem. Soc, Dalton Trans.* **1979**, 1646-1650.
(57) Kilner, C. A.; McInnes, E. J. L.; Leech, M. A.; Beddard, G. S.; Howard, J. A. K.; Mabbs, F. E.; Collison, D.; Bridgeman, A. J.; Halcrow, M. A. A Crystallographic, EPR and Theoretical Study of the Jahn-Teller Distorsion in [$CuTp_2$] (Tp^- = Tris{pyrazol-1-yl}hydridoborate) *Dalton Trans.* **2004**, 236-243.
(58) Feher, R. Dissertation, Technische Universität München, 1996.
(59) Santana, M. D.; López-Banet, L.; García, G.; García, L.;Pérez, J.; Liu, M. Hydrogen Bonding and Anion Binding in Structures of Tris(pyrazolyl)boratenickel(II) and Phospate Esters *Eur. J. Inorg. Chem.* **2008**, 4012-4018.
(60) Krzystek, J.; Ozarowsky, A.; Telser, J. Multi-Frequency, High-Field EPR as a Powerful Tool to Accurately Determine Zero-Field Splitting in High-Spin Transition Metal Coordination Complexes *Coord. Chem. Rev.* **2006**, *250*, 2308-2324.
(61) Desrochers, P.J.; Telser, J.; Zvyagin, S. A.; Ozarovski, A.; Krzystek, J.; Vicic, D. A. Electronic Structure of Four-Coordinate C_{3v} Nickel(II) Scorpionate Complexes: Investigation by High-Frequency and -Field Electron Paramagnetic Absorption Spectroscopies *Inorg. Chem.* **2006**, *45*, 8930-8941.
(62) Desrochers, P.J.; Sutton, C. A.; Abrams, M. L.; Ye, S.; Neese, F.; Telser, J.; Ozarovski, A.; Krzystek, J. Electronic Structure of Nickel(II) and Zinc(II) Borohydrides from Spectroscopic Measurements and Computational Modeling *Inorg. Chem.* **2012**, *51*, 2793-2805.
(63) Rinkevicius, Z.; Vaara, J.; Telyatnyk, L.; Vahtras, O. Calculations of Nuclear Magnetic Shieldings in Paramagnetic Molecules *J. Chem. Phys.* **2003**, *118*, 2550-2561.
(64) Tierney, D. L. Jahn-Teller Dynamics in a Series of High-Symmetry Co(II) Chelates Determine Paramagnetic Relaxation Enhancements *J. Phys. Chem. A* **2012**, *116*, 10959-10972.

(65) Aubagnac, J.-L.; Claramunt, R. M.; Elguero, J.; Gilles, I.; Sanz, D.; Trofimenko, S.; Virgili, A. Structural Characterization of Paramagnetic Octahedral Homoscorpionate (Polypyrazolylborate) Cobalt Complexes by ^{1}H and ^{13}C NMR Spectroscopy and by FAB-Mass Spectroscopy *Bull. Soc. Chim. Belg.* **1995**, *104*, 473-482.
(66) All shifts reported in ref. 64 are about 3% smaller than those in Table 3 probably due to different temperature calibration.
(67) Myers W. K.; Scholes C. P.; Tierney D. L. Anisotropic Fermi Couplings Due to Large Unquenched Orbital Angular Momentum: Q-Band ^{1}H, ^{14}N, and ^{11}B ENDOR of Bis(trispyrazolylborate) Cobalt(II) *J. Am. Chem. Soc.* **2009**, *131*, 10421-10429.
(68) Myers W. K.; Duesler E. N.; Tierney D. L Integrated Paramagnetic Resonance of High-Spin Co(II) in Axial Symmetry: Chemical Separation of Dipolar and Contact Electron-Nuclear Couplings *Inorg. Chem.* **2008**, *47*, 6701-6710.
(69) Krzystek, J.; Zvyagin, S. A.; Ozarowski, A.; Fiedler, A. T.; Brunold, T. C.; Telser, J.Definitive Spectroscopic Determination of Zero-Field Splitting in High-Spin Cobalt(II) *J. Am. Chem. Soc.* **2004**, *126*, 2148-2155.
(70) Krzystek J.; Zvyagin S. A.; Ozarowski, A.; Trofimenko S.; Telser J. Tunable-Frequency High-Field Electron Paramagnetic Resonance *J. Magn. Reson.* **2006**, *178*, 174-183.
(71) Pavlov, A. A.; Nehrkom, J.; Pankratova, Y. A.; Ozerov, M.; Mikhalyova, E. A.; Polezhaev, A. V.; Nelyubina, Y. V.; Novikov, V. V. Detailed Electronic Structurfe of a High-Spin Cobalt(II) Complex Determined from NMR and THz-EPR Spectroscopy *Phys. Chem. Chem. Phys.* **2019**, *21*, 8201-8204.
(72) Benda L.; Mareš J.; Ravera E.; Parigi G.; Luchinat C.; Kaupp M.; Vaara J. Pseudo-Contact NMR Shifts over the Paramagnetic Metalloprotin CoMMP-12 from First Priciples *Angew. Chem. Int. Ed. Engl.* **2016**, *55*, 14713-14717.
(73) Krzystek, J.; Kohl, G.; Hansen, H.-B.; Enders, M.; Telser, J. Combining HFEPR and NMR Spectroscopies to Characterize Organochromium(III) Complexes with Large Zero-Field Splitting *Organometallics* **2019**, *38*, 2179-2188.
(74) Autillo, M.; Guerin, L.; Dumas, T.; Grigoriev, M. S.; Fedoseev, A. M.; Cammelli, S.; Solari, Pier L.; Guillaumont, D.; Guilbaud, P.; Moisy, P.; Bolvin, H.; Berthon, C. Insight of the Metal-Ligand Interaction in f-Element Complexes by Paramagnetic NMR Spectroscopy *Chem. Eur. J.* **2019**, *25*, 4435-4451
(75) Ott, J. C.; Wadepohl, H.; Enders, M.; Gade, L. H. Taking Solution Proton NMR to Its Extreme: Prediction and Detection of a Hydride Resonance in an Intermediate-Spin Iron Complex *J. Am .Chem. Soc.* **2018**, *140*,17413-17417.
(76) Pavlov, A. A.; Savkina, S. A.; Belov, A. S.; Voloshin, Y. Z.; Nelyubina, Y. V.; Novikov, V. V. Very Large Magnetic Anisotropy of Cage Cobalt(II) Complexes with a Rigid Cholesteryl Substituent from Paramagnetic NMR Spectroscopy *ACS Omega* **2018**, *3*, 4941-4946
(77) Hiller, M.; Krieg, S.; Ishikawa, N.; Enders, M. Ligand-Field Energy Splitting in Lanthanide-Based Single-Molecule Magnets by NMR Spectroscopy *Inorg. Chem.* **2017**, *56*, 5285-15294.
(78) Vonci, M.; Mason, K.; Suturina, E. A.; Frawley, A. T.; Worswick, S. G.; Kuprov, I.; Parker, D.; McInnes, E. J. L.; Chilton, N. F. Rationalization of Anomalous Pseudocontact Shifts and Their Solvent Dependence in a Series of C_3-Symmetric Lanthanide Complexes *J. Am. Chem. Soc.* **2017**, *139*, 14166-14172.
(79) Novotný, M.; Sojka, M.; Komorovsky, S.; Nečas, M.; Marek, R. Interpreting the Paramagnetic NMR Spectra of potential Ru(III) Metallodrugs: Synergy between

Experiment and Relativistic DFT Calculations *J. Am. Chem. Soc.* **2016**, *138*, 8432-8445.
(80) Brühl, M.; Ashbrook, S. E.; Dawson, D. M.; Doyle, R. A.; Hrobárik, P.; Kaupp, M.; Smellie, I. A. Paramagnetic NMR of Phenolic Oxime Copper Complexes: A Joint Experimental and Density Functional Study *Chem. Eur. J.* **2016**, *22*, 15328-15339.
(81) Mairena, M. A.; Urbano, J.; Carbajo, J.; Maraver, J. J.; Alvarez, E.; Díaz-Requejo, M. M.; Pérez, P. J. Effects of the Substitution in the Tp^xCu Activation of Dioxygen: An Experimental Study *Inorg. Chem.* **2007**, *46*, 7428-7435.
(82) Lopez, C.; Claramunt, R. M.; Sanz, D.; Foces, C. F.; Cano, F. H.; Faure, R.; Cayon, E.; Elguero, J. Structure of Bis-, Tris- and Tetrakispyrazolyborates in the Solid State (Sodium and Potassium Salts of Tetrakispyrazolylborate by X-Ray Crystallography) and in Solution (^{1}H, ^{11}B, ^{13}C and ^{15}N NMR) *Inorg. Chim. Acta* **1990**, *176*, 195-204.
(83) Domaille, P. J. Direct Measurement of the Electron Susceptibility Anisotropy in Paramagnetic Complexes Using High-Field Deuterium NMR *J. Am. Chem. Soc.* **1980**, *102*, 5393-5396.
(84) Bothner-By, A. A.; Domaille, P. J.; Gayathri, C. Ultra-High-Field NMR Spectroscopy: Observation of Proton-Proton Dipolar Coupling in Paramagnetic Bis[tolyltris(pyrazolyl)borato]cobalt(II) *J. Am. Chem. Soc.* **1981**, *103*, 5603-5604.
(85) Kuck, M.; Wadepohl, H.; Enders, M.; Gade, L. H. *Chem. Eur. J.* **2013**, *19*, 1599-1606.
(86) Köhler, F. H. In *Magnetism: Molecules to Materials*; Miller, J. S., Drillon, M., Eds.; Wiley-VCH: Weinheim, Germany, 2001; Vol. *I*, Chapter 12.
(87) Kasansky, L. P.; McGarvey, R. B. NMR and EPR Spectroscopies and Electron Density Distribution in Polyoxoanians *Coord. Chem. Rev.* **1999**, *188*, 157-210.
(88) Bertini, I.; Luchinal, C.; Rarigi, G. Pieratelli, R. NMR Spectroscopy of Paramagnetic Metalloproteins *ChemBioChem* **2005**, *6*, 1536-1549.
(89) Walker, F. A. In *Handbook of Porphyrin Science*; Kadish, K. M.; Smith, K. M.; Guilard, R., Eds.; World Scientific: Singapore, **2010**, *6*, 1-337.
(90) Köhler, F. H. In *Encyclopedia of Magnetic Resonance*; Harris, R. K.; Wasylishen, R. E., Eds.; John Wiley & Sons, Ltd.: Chichester, **2012,** *6*, 3293-3309.
(91) Rouf, S. A. Dissertation, University of Oulu, 2017.
(92) Vaara, J. Theory and Computation of Nuclear Magnetic Resonance Parameters *Phys. Chem. Chem. Phys.* **2007**, *9*, 5399-5418.
(93) Bühl, M. Density Functional Computations of Transition Metal NMR Chemical Shifts: Dramatic Effects of Hartree-Fock Exchange *Chem. Phys. Lett.* **1997**, *267*, 251-257
(94) Pennanen, T. O.; Vaara, J. Nuclear Magnetic Resonance Chemical Shifts in an Arbitrary Electron Spin State *Phys. Rev Lett.* **2008**, *100*, 133002.

For Table of Contents use only

SYNOPSIS

The large ^{1}H, ^{13}C, ^{11}B, and ^{14}N NMR signal shifts of paramagnetic complexes with popular Tp ligands are reproduced by first-principles calculations. This supports the signal assignment and thus efficient characterization of the compounds. Hints to best-suited central-metal ions and NMR nuclei as well as information on underlying g factors, zero-field splittings, and structures are provided. The spin crossover of Tp_2Fe is analyzed.

TOC GRAPHIC

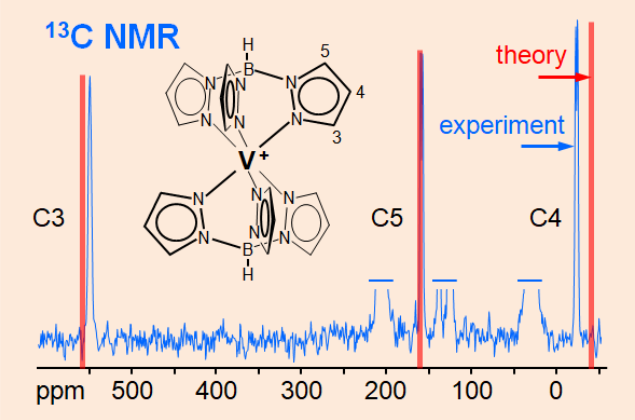

KEY WORDS

Pyrazolylborates, paramagnetic NMR, first-principles calculations